Electronic Thesis and Dissertation Repository

8-23-2013 12:00 AM

Numerical Investigation of the Interdependence between Humeral Implant Position and Bone Removal Amount for Total Elbow Arthroplasty

Alexander J. Heroux
The University of Western Ontario

Supervisor
Dr. Remus Tutunea-Fatan
The University of Western Ontario Joint Supervisor
Dr. Shaun Salisbury
The University of Western Ontario Joint Supervisor
Dr. Ahmad Barari
The University of Western Ontario

Follow this and additional works at: https://ir.lib.uwo.ca/etd

© Alexander J. Heroux 2013

Part of the Bioimaging and Biomedical Optics Commons, Biomechanical Engineering Commons, and the Biomedical Devices and Instrumentation Commons

NUMERICAL INVESTIGATION OF THE INTERDEPENDENCE BETWEEN
HUMERAL IMPLANT POSITION AND BONE REMOVAL AMOUNT FOR TOTAL
ELBOW ARTHROPLASTY

by

Alexander James <u>Heroux</u>

Graduate Program in Biomedical Engineering

A thesis submitted in partial fulfillment
of the requirements for the degree of
Master of Engineering Science

The School of Graduate and Postdoctoral Studies
Western University
London, Ontario, Canada

© Alexander James Heroux 2013

ABSTRACT

Total elbow arthroplasty is a surgical procedure used to replace an afflicted articulation with prosthetic joint components. A good alignment between the native and prosthetic flexion-extension axes of the elbow is required to preserve its functionality. However, this is often unobtainable because of the mismatch between humeral canal and implant stem geometries. To correct this, surgeons are often required to intraoperatively make error-prone decisions when determining an appropriate implant posture that minimizes the amount of cortical bone to be removed while maintaining the alignment between the two flexion-extension axes. To address this issue, the present study has developed computational tools to be used preoperatively to assess the relationship between bone removal and implant malalignment magnitudes; the overall objectives being related to their individual or simultaneous minimization. The results presented determine an optimized implant position for 3 bone samples minimizing the implant interference and implant malalignment.

Keywords: total elbow arthoplasty; flexion-extension (FE) axis; implant malalignment; implant posture; humeral bone removal; numerical optimization

ACKNOWLEDGMENTS

TABLE OF CONTENTS

LIST OF TABLES

LIST OF FIGURES

LIST OF ABBREVIATIONS

α_{FE} - Flexion-extension rotation angle of the implant

α_{IE} - Internal-External rotation angle of the implant

α_{IH} - angle by which the implant coordinate system rotates upon to align to the humeral coordinate system

α_{VV} - Varus-valgus rotation angle of the implant

A_i^{imp} - Area of the whole implant cross section per CT slice

A_i^{int} - Interfering area per CT slice

$\mathcal{B}$ - Bins of categories

B-Rep - Boundary representations

CAD - Computer assisted design

CCW- counterclockwise

CPU - Computer Processing Unit

CT - Computed Tomography

CW - clockwise

$\mathcal{D}$ - Subset of data points analyzed

Δ - Global interference metric

δ_s - Maximum amount of interference per CT slice

DOF - degrees of freedom

$\mathcal{DT}$ - Delaunay Triangulation

DICOM - Digital Imaging Communications in Medicine

E_j^i - Characteristic edges formed from the characteristic vertices

f_{int} - Interference objective function

f_{mal} - Malalignment objective function

f_{MO} - Multi-objective function

FE - Flexion-extension

HCS - Humeral coordinate system

ICS - Implant coordinate system

IE - Internal-External

MRI - Magnetic resonance imaging

$n_{\mathcal{B}}$ - Number of bins

$\hat{\mathbf{n}}_{IH}$ - vector by which the implant coordinate system rotates upon to align to the humeral coordinate system

NN - Nearest Neighbour

$\boldsymbol{\Omega}_\text{I}$ - Implant 6 degree of freedom posture

$\mathbf{O}_\text{I}$ - Implant orientation

$\mathcal{O}_C$ - Outer Contour

$\mathbf{P}_{\text{E}_j^i}$ - Parametric lines forming the characteristic edges

$\mathbf{P}_\text{I}$ - Implant position

P_j^{cand} - Neighboring triangulated vertices

P^{curr} - Current point identified on the outer contour

P^{next} - Next point of the outer bone boundary

σ - Standard deviation

σ^2 - Variance

$\mathbf{T}_{\Omega_\text{I}}$ - Transformation matrix applied to the implant coordinate system

TEA - Total Elbow Arthroplasty

V_j^i - Characteristic vertices on the implant corners

V^{imp} - Total volume of the implant stem

V^{int} - Volume of stem interference per implant posture

VTK - Visualization Toolkit

VV - Varus-Valgus

X_{CC} - X translation of the implant

Y_{CC} - Y translation of the implant

y_i - Function value of a data point

$\bar{y}$ - Mean of the function values

$\hat{y}_i$ - Expected function value

Z_{CC} - Z translation of the implant

z_{CT} - Distance between CT slices

CHAPTER 1
INTRODUCTION

1.1 MOTIVATION

Total elbow arthroplasty (TEA) surgery is a surgical procedure performed on the upper limb in order to remedy excessive damage to the elbow joint indicated by joint pain, stiffness, or instability. A prosthetic device is used to replace the native bone to restore proper articulation in the elbow joint. Elbow arthroplasty surgery is not as common as a knee or a hip arthroplasty surgery. As a result, surgeons are not exposed to the surgery as often, resulting in insufficient experience with the procedure[1,2,3]. However, a growing trend in upper extremity arthroplasty surgeries, namely that this lack of exposure, causes some problems with the surgical protocol[2,3,4].

One of the primary goals of TEA is to replace the poor articulation with a prosthetic device that is capable to mimic most, if not all, of the kinematic functions of its native counterpart. To ensure this, the flexion-extension (FE) axis of the prosthetic elbow has to be aligned, to the largest extent possible, with the native FE axis of the articulation[5,6,7]. However, this goal is often not attainable in the surgical practice due to the geometric restrictions imposed by the shape of the medullary canal of the humerus on the position and orientation of the implant. As such, the implant alignment is often sacrificed in order to allow an acceptable insertion of the implant into the humeral canal[8,9]. Consequently, if the implant is not properly aligned with the native FE axis, eccentric loading through the implant will occur and this might lead to aseptic loosening of the prosthetic device[1].

Presently, the reported complication rates are anywhere from 8% to 32%.[4,10,11,12,13,14,15] These complications include: aseptic loosening, delayed avulsions, infection, and neuropathy. If aseptic loosening implant and/or articular pain are present, revision surgeries are often required to either reposition or replace the implant. It is important to note that revision rates for TEA surgery are on the rise, increasing from 11.5% in 1990 to 52.1% in 2005[16]. Along the same lines, other authors have indicated that from 1993 to 2007, there have been rising costs of TEA surgeries and revision surgeries with a 66% and a 100% increase respectively[4]. Furthermore, if excess loads are placed on the implant, this could result in implant or bone fractures. In this regard, Throckmorton et al. have determined that 5.8% of TEA patients had component fractures and 4.7% of patients had periprosthetic fractures[17].

On the other hand, if implant alignment is strictly enforced, it is very likely that certain amounts of cortical bone will have to be removed from the humeral canal in order to permit the attainment of a particular posture (*e.g.* position and orientation) of the humeral implant that practically enables a good match between prosthetic and native FE axes. However, it is reasonable to believe, in this case, that the weakened bone may not be able to take the required functional loads and this will result in fracture and/or further elbow joint damage. Obviously, this shortcoming can be partially alleviated through an allograft, but this is typically not regarded as a desirable solution due to its increased susceptibility to further complications such as infections or immune rejections[18]. Therefore, the amount of cortical bone to be removed should be minimized in order to preserve as much as possible the original strength of the native humerus.

Based on the discussion above, it becomes apparent while the attainment of the best possible alignment between the native and prosthetic FE axes as well as the removal of the minimal amount of cortical bone are both equally desirable traits of a TEA procedure, it can be inferred that they are in fact almost mutually exclusive conditions. Because of this, the surgeons often have to determine the best tradeoff between them; a task that is almost impossible to accomplish without adequate computational tools.

1.2   OBJECTIVE

The principal objective of this work is the development of computationally efficient preoperative planning tools that are capable to simultaneously take into consideration the amount of implant malalignment as well as the amount of interference between implant stem and humeral bone. The computational techniques to be developed are meant to support the planning stages of the TEA surgery by providing the surgeon with means to assess the position and amount of the cortical bone to be removed from the medullary canal in order to allow a superior alignment between the native and prosthetic FE axes. Furthermore, the computational tools and techniques to be developed are meant to provide further insight on the relative balance between the two aforementioned metrics, an aspect that was rarely – if ever – investigated by the surveyed literature.

1.3   HYPOTHESIS

The present study hypothesizes that superior elbow implant alignments can be acquired by means of controlled and precise removal of the cortical bone from the medullary canal of the humerus. To enable the verification of the proposed hypothesis, several tasks/aims to be sequentially accomplished are envisioned as follows:

i) extraction of discrete (*e.g.* point-based) inner and outer bone contours from CT data; ii) development of adequate metrics to be used in quantification of the implant malalignment as well as that of the implant interference condition; iii) development of computationally-efficient tools capable to optimize one or both metrics to be developed within acceptable bounds of variation for clinically-relevant constraints.

1.4   CONTRIBUTIONS

The original contributions brought by this thesis are related to the development of several numerical techniques and/or algorithms capable to accomplish the targeted tasks. While the majority of these developed techniques were based on relatively standard geometric or numerical procedures, several new computational methods were developed to automatically extract inner and outer bone boundaries directly from discrete clouds of points and to quantify the amount of interference between the implant stem and cortical bone in the context of discrete point-based data.

Moving to a higher level, this work is one of the first attempts made to demonstrate that implant malalignment and bone/implant interference amounts are in an relationship of inverse proportionality. As such, by means of computational tools identical or similar to those presented in this thesis and used in a preoperative setting; more correctly positioned elbow implants will ensure a higher success rate for TEA surgeries.

1.5   OUTLINE

Chapter 2 outlines background information pertaining to this thesis. In this context, an overview of the anatomy and physiology of the elbow will be presented along

with some fundamental concepts related to CT image acquisition of the osseous elbow configuration. Chapter 3 contains information on the generation of discrete (*e.g.* point-based) representations of the inner and outer humeral geometry, both performed by assuming a CT based data input. Chapter 4 is focused on the development of a computational technique capable to outline constrained implant postures to ensure minimal removal of the cortical bone. Chapter 5 turns the implant posture into an optimization objective, such that the efficiency of dual optimization techniques will be discussed in this context and finally, the thesis concludes with a chapter of conclusions.

CHAPTER 2
BACKGROUND

2.1 BIOLOGICAL PLANES

When referencing the body, it is important to establish anatomical directions and planes in order to further describe the location of reference. The major anatomical planes are the coronal (frontal), sagittal (lateral), and transverse planes. Within the coronal plane are posterior and anterior directional terms. Posterior refers to a direction to the back or behind and the anterior direction is towards the front. In the sagittal plane, there are the medial and lateral motions where the medial is towards the middle of the body and lateral is away from the middle of the body. Finally, the normals to the transverse plane make up the superior and inferior anatomical directions where superior is above and inferior is below the body. These terms can be visualized in Figure . Another important directional term not shown in Figure is distal and proximal. Distal refers to away from or farther from the origin, whereas proximal means near or closer to the origin. These terms are used throughout the following text and it is important to have a basic understanding of these definitions.
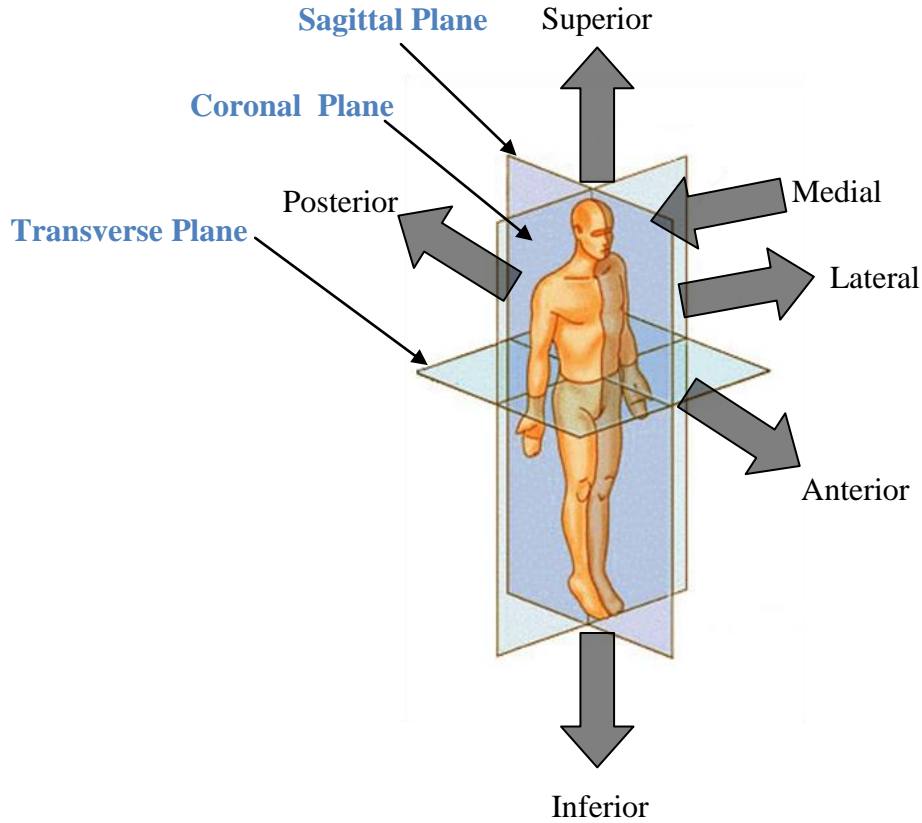
Figure 2.1: Anatomical planes and directions

2.2   ELBOW BIOMECHANICS

The upper extremity plays an extremely important role in day to day activities of an individual. Among upper limb's joints, the medially placed synovial hinged joint, called the elbow, enables the attainment of a broad palette of positions for the hand simply by modifying the intrinsic length of the upper extremity. Evidently, understanding the biomechanics of the elbow joint is of paramount importance when considering design considerations for surgical operations of the joint. Without adequate background on osteology, muscles and ligaments as well as elbow kinematics, the success of the elbow replacement procedure is improbable.

2.2.1   **Osteology**

The osseous structure of the elbow consists of three articulating bones, namely: the humerus, ulna, and radius. The humerus is a long bone connecting the shoulder to the elbow whereas the ulna and the radius connect the elbow to the wrist. The radius is positioned lateral of the ulna in the supinated position. Furthermore, the elbow joint is comprised of the distal humerus, proximal ulna, and proximal radius. The articulating components of the elbow include the trochlea and the capitellum on the distal humerus and the proximal ends of the ulna and the head of the radius. These articulations are named radiohumeral, ulnohumeral, and the radioulnar joints[19].

From a kinematic standpoint, the elbow has two degrees of freedom: flexion-extension and supination-pronation. The radiohumeral and ulnohumeral joints articulate with each other during flexion-extension and the radioulnar articulates during forearm rotation (Figure 2.2)[19].
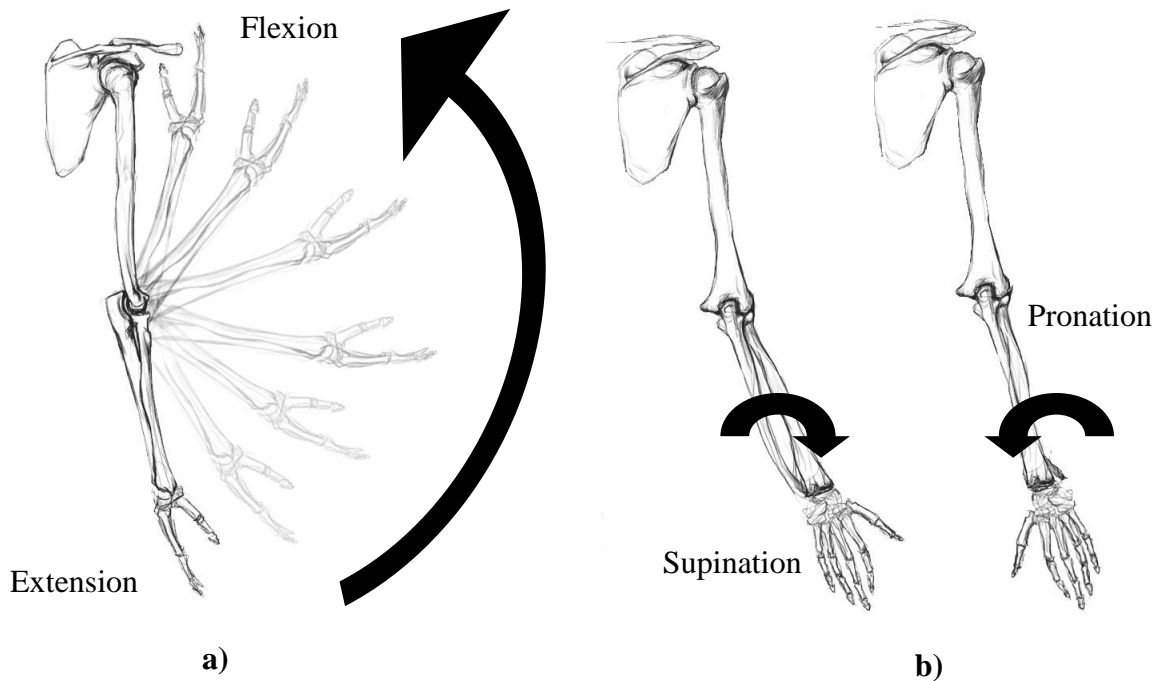
Figure 2.2: **a)** Flexion-extension movement of the elbow **b)** Pronation-supination
movement of the elbow

Traditionally, the primary functionality of the elbow is associated with that of a hinge joint. However, more recent studies seem to suggest that the elbow behaves more as a 3D helical joint since the FE axis translates in the sagital plane when moving from the flexion to the extension position[20]. Despite this, most researchers tend to agree that for the purpose of identifying the FE axis, it can be assumed that its direction remains unchanged except perhaps when the angle reaches its extremes[19,21,22,23]. Therefore, according to a very broad consensus FE axis is defined as the line joining the center of the spherical capitellum with the geometric center of trochlea sulcus, typically assimilated with a circular feature[1,5,8, 21,22,24,25, 26,27].

2.2.2   Elbow Movement

The axis of forearm rotation passes through the convex head of the radius in the proximal radioulnar joint and through the convex articular surface of the ulna at the distal radioulnar joint. Supination is defined as a rotation that forces the palms of one's hand to face upwards whereas pronation is the rotation forces the palms downwards. The range of motion achievable through supination and pronation has been shown to be 85 and 75 degrees respectively (Figure 2.2b).

Varus-Valgus motion is movement of the elbow in the coronal (frontal) plane (Figure). This motion is also referred to forearm abduction and adduction. The stability of the elbow joint is often measured by a varus-valgus stress test by physicians or orthopedic surgeons. A normal elbow has been estimated to have approximately 11.2 degrees of valgus motion and 6.6 degrees of varus motion[28].

As indicated above, the primary flexion-extension motion is linked into the hinge-like functionality of the elbow. However, during the flexion extension motion, the center of rotation has been observed to translate up to 7.8 mm distally and 2.5 mm laterally. As a result, the real flexion extension movement is slightly helical. Nevertheless, from a practical perspective these changes are rather minimal such that they are often disregarded; which means that elbow kinematics is similar to that of an idealized hinge. The ranges of motion of a typical elbow joint are 0 degrees in extension and 150 degrees in flexion[19].

2.3   ELBOW IMPLANT

One of most common techniques used to restore the lost functionality of the elbow involves its replacement with a prosthetic device called an elbow implant. While several manufacturers exist on the market, this study was performed in its entirety in the dimensional context of the implants fabricated by Tornier.

The latest line of Latitude EV total elbow prosthesis implants incorporate few enhanced design features (Figure 3). To offer highly customizable solutions that would better fit the broad dimensional/anatomical variety of joints encountered in the population, the implant is available in a modular format consisting of four principal sizes (*e.g.* from small to extra-large) of the humeral spool, humeral stem, ulnar stem, ulnar caps, radial heads, and radial stems. Other adjustable and/or dimensionally variable features on the implant could include: an optional linkage between the radial and the humeral component, anterior flanges for bone graft, square shaped stems or lateral fins to assist rotational stability. Furthermore, a titanium plasma spray is coated onto the lateral sides of the stem to ensure a superior long term fixation by facilitating the bone in-growth and high-density polyethylene is used to ensure smooth movements and avoid metal on metal contact between various components of the implant assembly[29].

Humeral
Component

Radial
Component

Hinged Joint

Ulnar
Component
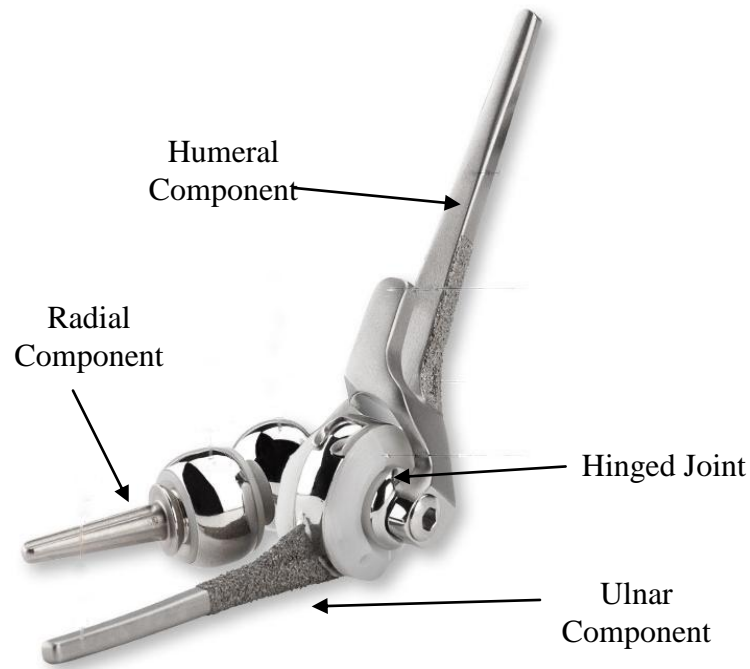
Figure 2.3: Tornier Latitude total elbow arthroplasty implant[29]

2.4   MEDICAL IMAGING

Medical imaging is primarily focused on the acquisition of internal anatomical details to be subsequently used by physicians for diagnosis and treatment purposes. There are many different techniques available to create the images such as: X-ray, computed tomography (CT), magnetic resonance imaging (MRI), positron emission tomography, single-photon emission computed tomography, and ultrasound. In the orthopaedic field, X-rays are widely used both because of the good contrast of the images generated and because of the relatively low cost of the procedure.

2.4.1   X-ray Imaging

The generation of the X-ray images (Figure 2.4) requires a source, a patient, as well as recording film. The X-ray source is aimed at the patient and some of the rays get

absorbed, reflected, or pass through the body unaffected. The film on the other side of the patient records the attenuation of the X-rays and the more X-rays reaching the film, the darker the image is. As a result, if a lot of rays are absorbed in the body, the film will remain white. Different parts of the body have different absorption rates thus have expected contrasts on the X-ray film. These varying absorption rates assist physicians in assessing the areas of concern in the body. The resolution of the image is dependent on a number of acquisition parameters among which the most important ones are the peak kilovoltage or beam energy, tube current, and exposure time. In order to increase the resolution of the image, an increase in these scanning parameters is necessary. However, that comes at the cost of exposing the patient to more radiation[26,30].

Figure 2.4: X-ray of a post-operative total elbow arthroplasty surgery.

2.4.2   **Computed Tomography (CT) Scanning**

CT scanning constitutes a newer and enhanced version of the X-ray technique in which images are acquired by means of a rotating X-ray source. Unlike X-rays that are generally capable to create only single 2D representations, CT scanners typically output multi-sliced X-ray images of the analyzed body anatomy. Cross-sectional images are subdivided into three dimensional pixels called voxels. For CTs, the resolution of the image depends on the scanning parameters used as well as the slice thickness. The resulting images can be computationally processed to render these 2D images into a 3D volumetric object whose geometry is easier to understand and analyze (Figure 2.5)[26,30,31].
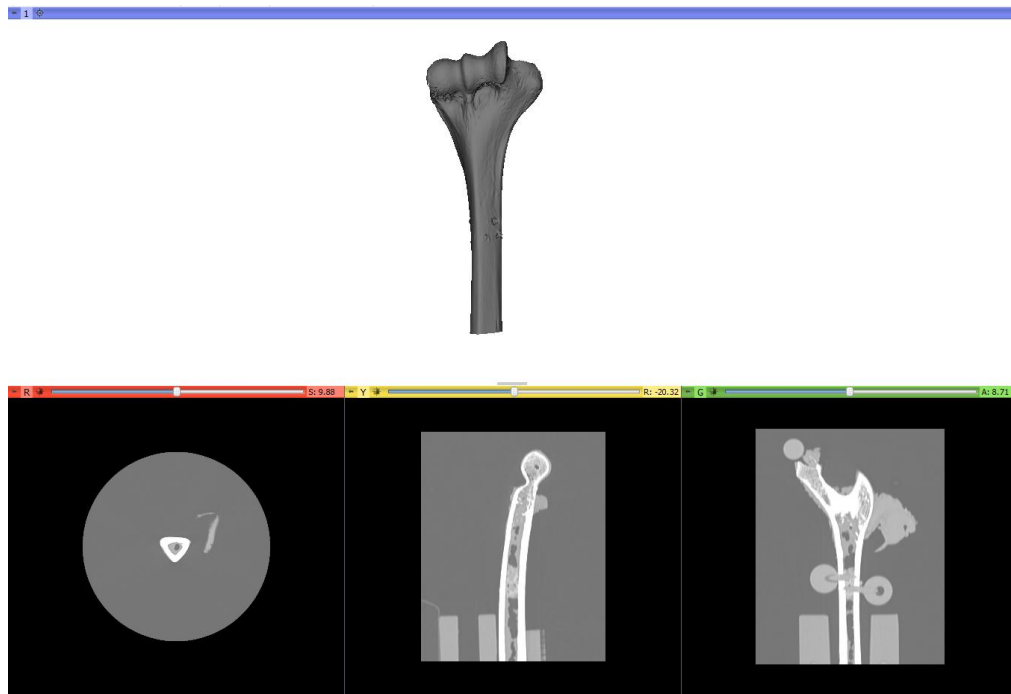
Figure 2.5: 3D Slicer screenshot of bone sample 1. 3D rendered volume (top), transverse plane (bottom left), sagittal plane (bottom middle), and coronal plane (bottom right)

2.4.3 **DICOM**

Since the inception of medical imaging, the amount of information generated, processed, and then stored through various body-scanning techniques has experienced an explosive growth. However, not long after the wide scale clinical adoption of CT scanners in the 1970s, it was noticed that there is a need to standardize the format in which digital images were generated by different imaging devices manufactured by various OEMs. The intended standardization was meant to facilitate the access of all interested stakeholders to CT scanning-acquired information as well as to enable its various forms of processing, as related to visualization, reading, exchange, etc.

As such, the American College of Radiology (ACR) and the National Electrical Manufacturers Association (NEMA) formed in 1983 a joint committee whose objective was to develop a format capable to encode in the same manner the imaging data regardless of the equipment used to acquire it. As a result of that initiative, the Digital Imaging and Communications in Medicine (DICOM) standard was created.

Currently, the standard includes a file format definition and a communications protocol enabling the integration of scanners, servers and printers which might become involved in various phases of data processing protocol. This universal picture archiving and communication system (PACS) provides an efficient means to store and transfer medical images across different imaging modalities[32]. One of the most important features of DICOM standard resides in the fact that patient ID is part of the data set of the DICOM image so that the two cannot be separated from each other, even when the data has to be anonymized for bioethical reasons[33].

2.5   TOTAL ELBOW ARTHROPLASTY

Total elbow arthroplasty (TEA) is a surgical procedure aiming to address and/or correct various pathological conditions associated with rheumatoid arthritis, elbow joint injuries, elbow joint instability, and severe joint pain. The primary goal of the procedure is to replace one of the major articulations of the upper limb with a prosthetic device aiming to restore, to the highest degree, most of the lost functionality of its native counterpart. Since the overall incidence of TEA is relatively low compared to that of other joint arthroplasties, most orthopaedic surgeons tend to have insufficient exposure to the procedure and this in turn translates into their inadequate familiarity and proficiency with the process. As such, TEA patients often have to return for subsequent revision surgeries caused by the failure associated with the aseptic loosening of their implants

spool shaped trochlear sulcus[5,8,24,27,36,37,38]. Since the capitellum and trochlea sulcus are acknowledged as two of the most important anatomical features of the distal humerus geometry, the humeral spool was designed in such a way to mimic them as close as possible (Figure 2.6b). Furthermore, many TEAs require the excision of the distal portion of the humerus in order to allow an appropriate insertion of the implant within the endosteal canal.
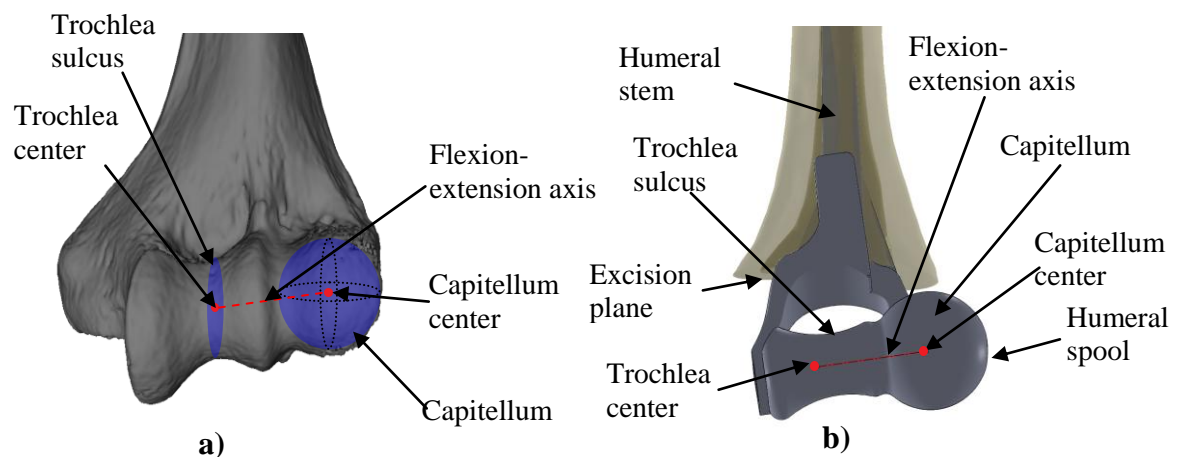
Figure 2.6: Significant anatomical features of the distal humerus: **a)** native geometry, and **b)** prosthetic replica.

As it can be inferred, most of the implant installation challenges are related to the humeral link, and they are caused by the large length of the stem to be inserted and then cemented within the canal. Various combinations of broaches and/or reamers are used to enlarge the canal in order to facilitate implant insertion which is often impossible otherwise[39,40]. The amount of bone to be removed varies from one individual to the other since it is strongly dependent upon the local anatomy of articulation to be replaced as well as the size of the implant to be used[29,41]. Given that elbow implants are generally

produced in three to four standard sizes ranging from small to extra large[37], the probability of an ideal match between the available sizes and humeral geometry is relatively small in current clinical practice. Regardless of the implant size selected, the amount of cortical bone to be removed should be minimized at all costs in order to avoid: i) the extensive use of bone cement, which often leads to non-ideal loading conditions of the implant, and ii) substantial thinning and/or penetration of the cortical wall of the humerus[42,43]. Appropriate measures have to be taken to limit the amount of malalignment between the native and prosthetic FE axes of the elbow in order to warrant the long term success of the surgical procedure and thereby improve the overall patient outcomes and quality of life.

In the current clinical practice, most of the canal enlargement operations rely heavily on the expertise of the surgeon performing the TEA procedure. Both reaming and broaching of the humeral canal are typically performed in a "blind" or "semi-blind" manner due to the lack of intraoperative means to visualize the instantaneous location of the contact between the cutting tool and bone. Furthermore, since the anatomical diversity of the humeral geometry makes each implantation procedure unique, it is not uncommon that canal enlargement operations pose significant difficulties even to experienced surgical professionals.

2.6   COMMON COMPLICATIONS OF TOTAL ELBOW ARTHROPLASTY

Complications often arrive intra-operatively and/or post-operatively after a total elbow replacement procedure. The complications are widely publicized and have a relatively large incidence. This large incidence can be attributed to the elbow joint being

a complex joint having poor soft-tissue coverage, a common site affected by rheumatoid arthritis or post-traumatic arthritis, and is transversed by the ulnar nerve. A recent literature study done on the incidence of complications of total elbow arthroplasty revealed a complication rate of 27.9%. Complications requiring another surgical procedure relating to TEA surgery include: aseptic loosening, infection, ulnar nerve lesions, disassembly of the implant, dislocation, intraoperative fractures, and prosthetic fractures[13,19].

Aseptic loosening is more prominent in linked or constrained devices. These particular devices are highly stable at the ulna-humeral joint. Studies have shown incidence rates from 7-17%[44,45,46,47]. This stability inherently causes large transmitted loads to the stem components of the ulna and the humerus. These high loads affect the bone-cement interface. As a result, semi-constrained and unconstrained devices are more prominently used. Unfortunately there exists a tradeoff between implant stability and implant loosening in the case of current elbow prosthetic implants, thus the stability of an unconstrained joint is compromised for better aseptic loosening rates[13,19].

Infection of the elbow joint post-operatively is a major concern for patients. Some studies indicated complication rates as high as 7-8%. However recent surgical techniques utilizing antibiotic-impregnated cement have lowered these incident rates to 1-2.5%[19]. Treatment of an infected elbow include placement of antibiotic beads, removal and reimplantation of components, or resection arthroplasty. Orthopaedic surgeons typically decide to perform a resection due to the limited information on which to base treatment decisions upon[13,19].

The incidence of nerve damage as a result from the total elbow arthroplastic surgery has been reported in the past to be as high as 26% of TEA patients[48,49]. More recent studies have shown that ulnar neuropathy was found to be as low as 2.5%. The reduction in incidence can be attributed to an improvement of the surgical procedure and a routine ulnar nerve transposition during the surgery[50]. Fortunately, the symptoms generally subside within 2 to 6 weeks post operatively[44,51,52].

Bushing wear in the implant ulna-humeral joint has been a major problem and ranged between 5-12% in frequency. Recent design iterations have limited this frequency creating more stable elbow prosthetics. In linked prosthetic designs, problems tend to occur when the pin, linking the humeral and ulna components, becomes loose and this leads to implant failure to be rectified through a revision surgery. However, the degree of difficulty required by the surgical replacement of bushings and other small components is relatively low since the majority of elbow implant remains intact and stable. Other wear issues include high-density polyethylene debris and metallic synovitis. High density polyethylene wear is treated by removing and replacing the articulation components. Also, the joint must be cleansed in order to remove any debris from the worn off polyethylene[13,19].

Perioperative bone fractures in the surrounding area of the implant result from implant loosening and insufficient bone stock. These fractures should be stabilized promptly in order to prevent any further implant loosening. Several Kutchner wires are used to fix the fractured fragments back to the native bone. While the perioperative fractures are being treated, the loose implant should also be treated to avoid any secondary loosening or other problems[13,19,53].

One of the major but relatively rare complications of TEA is caused by the mechanical failure/fracture of the humeral or ulnar stems and studies performed at Mayo clinic have attributed these fractures to traumatic arthritis. The complexity of the procedure involved by the replacement of the fractured stem is high, but its success rates are good[19].

CHAPTER 3

POINT-BASED REPRESENTATIONS OF HUMERAL BONE CONTOURS

3.1 OVERVIEW

The objective of the present chapter is to outline the numerical techniques which were developed to automatically generate point-based (*e.g.* discrete) representations of the bone geometry by starting off with an input consisting of CT-acquired scans of the humeral specimens. Given the broader scope of the current work, discrete representations of the geometry were preferred to those involving continuous representations, such as parametric curves, primarily due to the slightly more elevated complexity of the calculations involving point to curve computations.

As a counterargument to this decision, it is perhaps important to note here that, in general CAD terms, point-based representations are often considered inferior to those involving parametric formulations – *i.e.* curves or surfaces – due to their relative visualization ambiguity. However, in addition to the aforementioned computational efficiency, which was in fact the determinant decisional factor in case of the present work, it should also be reminded that in a wide majority of instances, point to curve or point to surface calculations eventually reduce themselves to the same to calculations of the Euclidian distance between two discrete points, such that the utility of point to parametric conversions is at least arguable given the fact that most curve fitting algorithms are accompanied by a number of errors. Another point to be reminded here is

that the array-based format which is inherently built within the CT data makes pixel to point conversion extremely straightforward.

3.2   GENERATION OF POLYGONAL MESH

The unequivocal identification of point-based representations for outer and inner boundaries of the cortical wall is essential for determining the relative position between implant and humeral points. In this regard, each of the implant points could occupy three distinct positions with respect to the bone: 1) within inner contour (i.e. inside of medullary canal, non-interfering condition), 2) between inner and outer contours (i.e. in interference condition), and 3) outside of outer contour (i.e. in penetration condition).
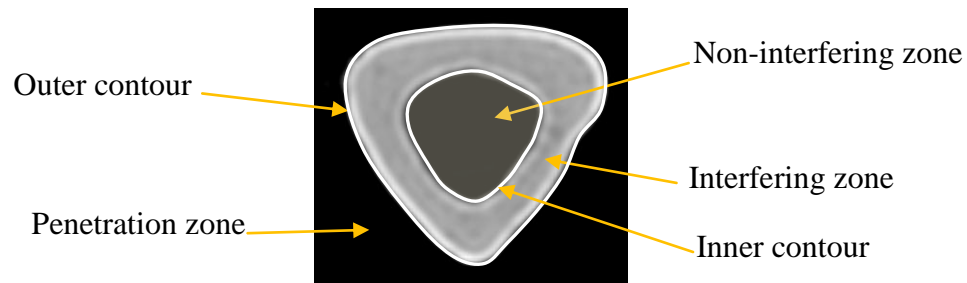
Figure 3.1: Relative positioning options for implant points with respect to bone.

The data constituting the primary input for the developed technique was prepared through a method routinely used by researchers in biomechanics to prepare 3D polygonal mesh models of the analyzed skeletal geometry. During this procedure, the stack of raw 2D data acquired by the CT scanner (Figure 3.2a) is initially reconstructed into 3D voxel-based format that can be visualized with a specific volume rendering method (Figure 3.2b). Then, in a second conversion step, the 3D voxelized representation is further processed to a polygonal mesh (Figure 3.2c) format through a standard technique; for

instance, marching cubes algorithm[54]. In this study, all investigated humeral specimens were converted through this technique to a commonly used mesh format called VTK; which constitutes the core of the Visualization Toolkit[55]. While a variety of software tools is available to complete these tasks, the present study relied on the latest version of Slicer3D freeware, in which segmentation parameters were set according to prior studies[38]. Once the VTK mesh data was created, only its vertices were retained for further processing. As Figure 3.2c suggests, a certain amount of triangular mesh vertices are generally positioned between the original CT scan planes. In order to minimize the amount of information loss caused by their elimination, all of the "vertex outliers" were projected/shifted to the closest CT plane based on their relative position with respect to mid-voxel plane.
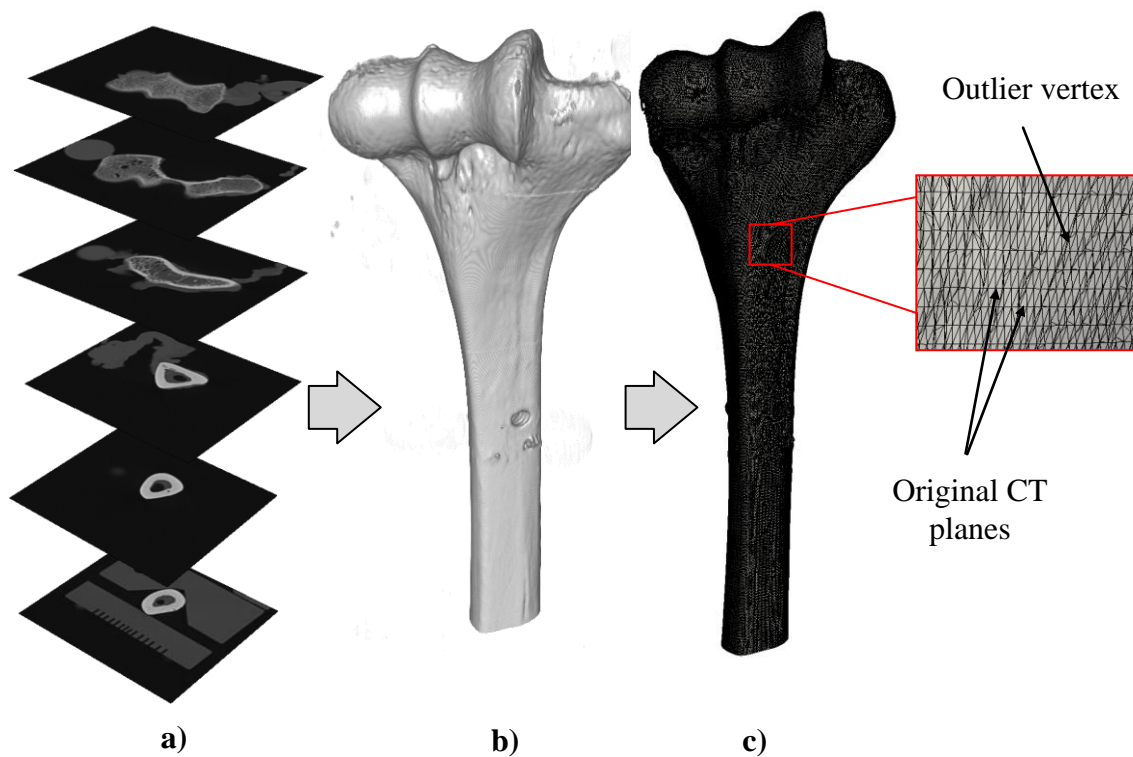
Figure 3.2: CT to polygonal mesh conversion of data for humeral specimens: **a)** stack of raw CT slices, **b)** rendered humeral volume, and **c)** triangular mesh generation.

3.3   EXTRACTION OF THE DISCRETE POINTS FROM MESH

Figure 3.3 shows a sample comparison between the original raw CT data and its corresponding points created at the end of the preprocessing phase to serve as input for cortical bone boundaries identification to be detailed throughout the next sections. As the presented sample suggests, most of the contour identification challenges are caused by the presence of irregular and randomly distributed "islands" in the preprocessed data caused either by bone defects/voids and/or other imaging artifacts due to the unintentional segmentation of the soft tissue. While a more application-oriented segmentation could potentially eliminate most of the soft tissue contours, relatively little can be done about the innate bone defects whose presence hinders an adequate

identification of the three main zones outlined in Figure 3.1 which is a critical step towards the computation of the interference amount experienced for a certain implant posture.
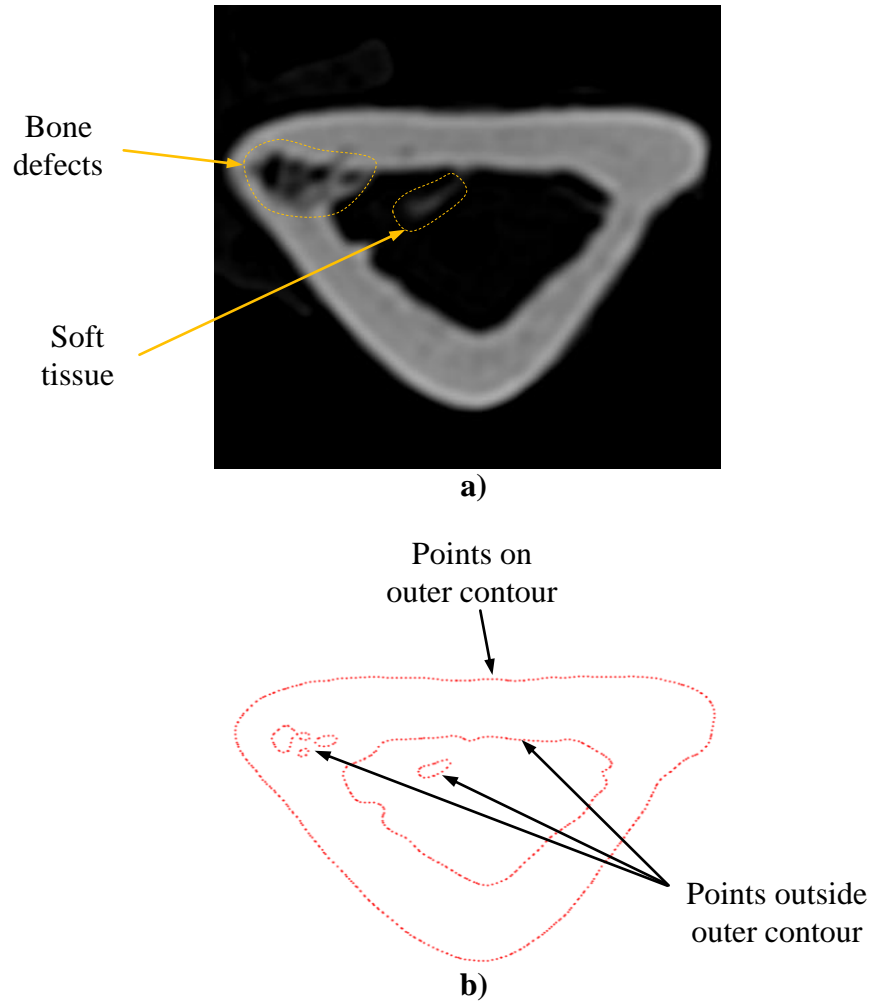
Figure 3.3: Correspondence between original CT and preprocessed data: **a)** original CT slice, and **b)** extracted mesh vertices.

3.4   GENERATION OUTER BONE CONTOURS

A quick but effective visual/qualitative analysis of the raw point-based dataset acquired suggests that preprocessing the distances between consecutive points on the

outer bone boundary are always smaller than those between inner contour points (Figure 3.3b). This can be interpreted as a consequence of different point density characteristics to bordering and internal zones of the cortical bone. With this observation in mind, outer bone contours have been determined by means of nearest neighbor (NN) approach which aims for the point that has the smallest Euclidian distance with respect to the currently analyzed location. To increase computational speed by avoiding unnecessary distance calculations, Delaunay triangulation ($\mathcal{DT}$) was first applied on the planar subset of data points analyzed ($\mathcal{D}$). This technique was used to speculate one of fundamental properties of $\mathcal{DT}$, namely that NN graph is one of its subsets. With this transformation, the raw unsorted and thus "amorphous" set of points $\mathcal{D}$ is being converted into an organized structure that is characteristic to Delaunay-type data (Figure 3.4a). In other words, if $P^{curr} \in \mathfrak{Dt}(D)$ is the current point identified on the outer contour $\mathcal{O}_C \subset \mathfrak{D}$ ($P^{curr} \in \mathcal{O}_C$), then the next point of the outer bone boundary ($P^{curr} \in \mathcal{DT}(\mathcal{D})$ and $P^{next} \in \mathcal{O}_C$) has to obey the following:

$$P^{next} = \left\{ P_m^{cand} \in \mathcal{DT}(\mathcal{D}) \Big| \left| \mathbf{P}_{P_m^{cand}} - \mathbf{P}_{P^{curr}} \right| = \min_{\forall j \leq n} \left(\left| \mathbf{P}_{P_j^{cand}} - \mathbf{P}_{P^{curr}} \right| \right), j \in \mathbb{N} \right\}$$

(3.1)

where P_j^{cand} are all n candidates neighboring triangulation vertices for the analyzed current point $P^{curr} (P^{curr} \in \mathfrak{Dt}(\mathfrak{D}))$ as shown in Figure 3.4b. Once P^{next} is been determined, the location of P^{curr} is updated to P^{next} and then the old P^{curr} is deleted to force the advancement along outer contour vertices. Obviously, the identification of outer contour points will stop once the point used to initialize the NN search – typically selected at $min(X)$ location – described above becomes equivalent with P^{next}. The

iterative applications of this technique on all preprocessed CT slices will generate an ordered and clean representation for outer boundaries of the investigated humeral specimen (Figure 3.4c).

a)

$$P_n^{cand}$$

$$\cdots$$

$$\cdots$$

$$P^{next} \equiv P_m^{cand}$$

$$P_1^{cand}$$

$$\cdots$$
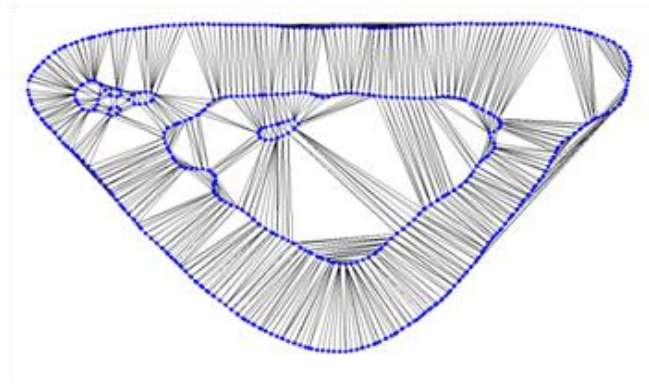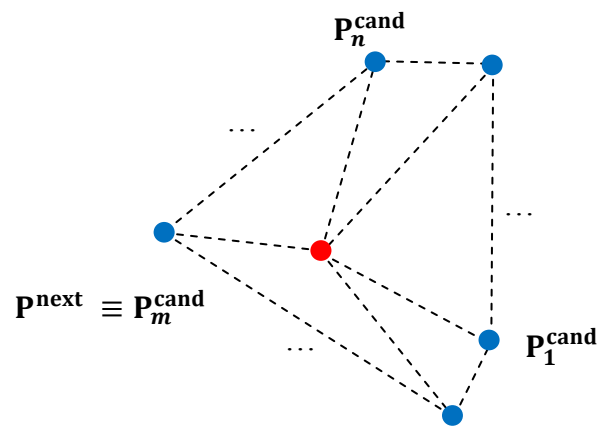
b)
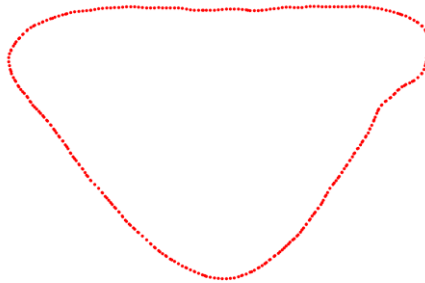
c)

Figure 3.4: Determination of point-based outer contours: **a)** Delaunay triangulation, **b)** nearest neighbor, and **c)** extracted final outer contour.

3.5   GENERATION OF THE INNER BONE CONTOURS

Despite of its robustness for outer boundaries, NN strategy failed to provide appropriate results for the more complex and convoluted geometry of the endosteal canal that often encompasses distanced regions of grouped points surrounding various bone defects and/or imaging artifacts as illustrated in Figure 3.5a. Although various combinations of NN techniques were tested, none of them seemed capable to identify the inner bone contour in a manner that is consistent with an intuitive user-driven selection (Figure 3.5a).

It is perhaps important to note here the underlying assumption behind the proposed inner bone contour is that only solid (*e.g.* 100% nonporous) cortical bone will be tested in this study for interference with implant geometry. The logical consequence of this assumption is that porous/trabecular (*e.g.* with voids or bone defects) zones will be assigned a zero stiffness, in a sense that if the inserted implant stem will come in contact with them, they will be crushed and thus eliminated. Obviously, while an inherent degree of subjectivity is associated with this hypothesis, it is believed that this represents an acceptable simplification of the investigated problem.

|a)|b)|
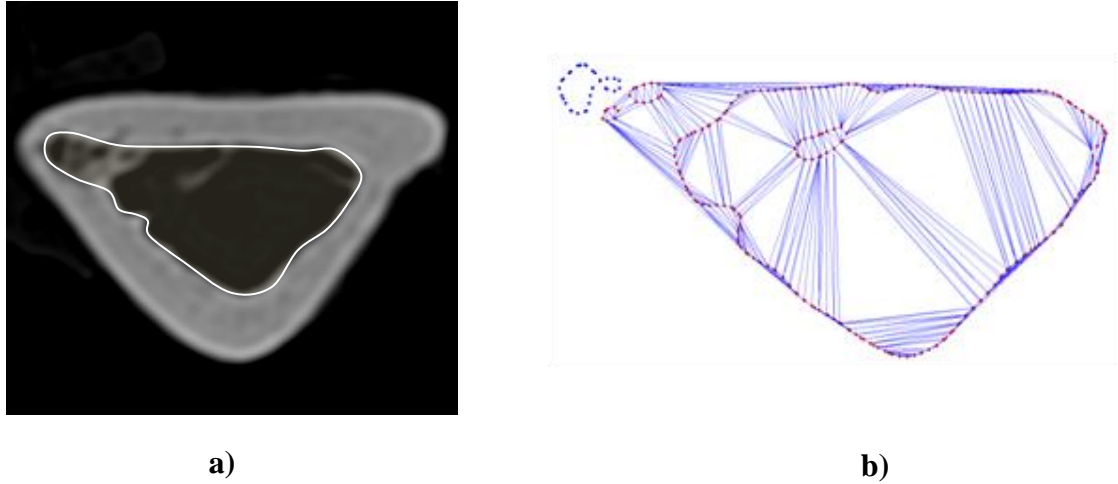
Figure 3.5: Expected and actual results for inner contours identified with nearest neighbor strategy: **a)** user-selected inner contour, **b)** incorrect "island-trapped" inner contour.

The most common cause of failure for NN approach was related to "trapping" of the search to one of the regionalized "islands" that are often present in the context of medullary canal walls. While from a theoretical standpoint, this issue could be solved through an appropriate merging of the previously identified regions/islands of point datasets, the actual implementation was found to be inefficient in case of high variability exhibited by inner contour data.

To remedy this issue, a completely different route was taken to extract the points on the inner bone contour ($I_C \subset \mathfrak{D}$). Essentially, all points that were left out after the elimination of outer contour points from the preprocessed planar datasets (Figure 3.3b) were divided into $n_\mathfrak{B}$ "bins" ($\mathfrak{B}$) of equal size as measured along the X direction (Figure 3.6a):

$$\Delta X_\mathfrak{B} = \frac{\Delta X_{max}}{n_\mathfrak{B}} = \frac{max_{I_C}(X) - min_{I_C}(X)}{n_\mathfrak{B}} \qquad (3.2)$$
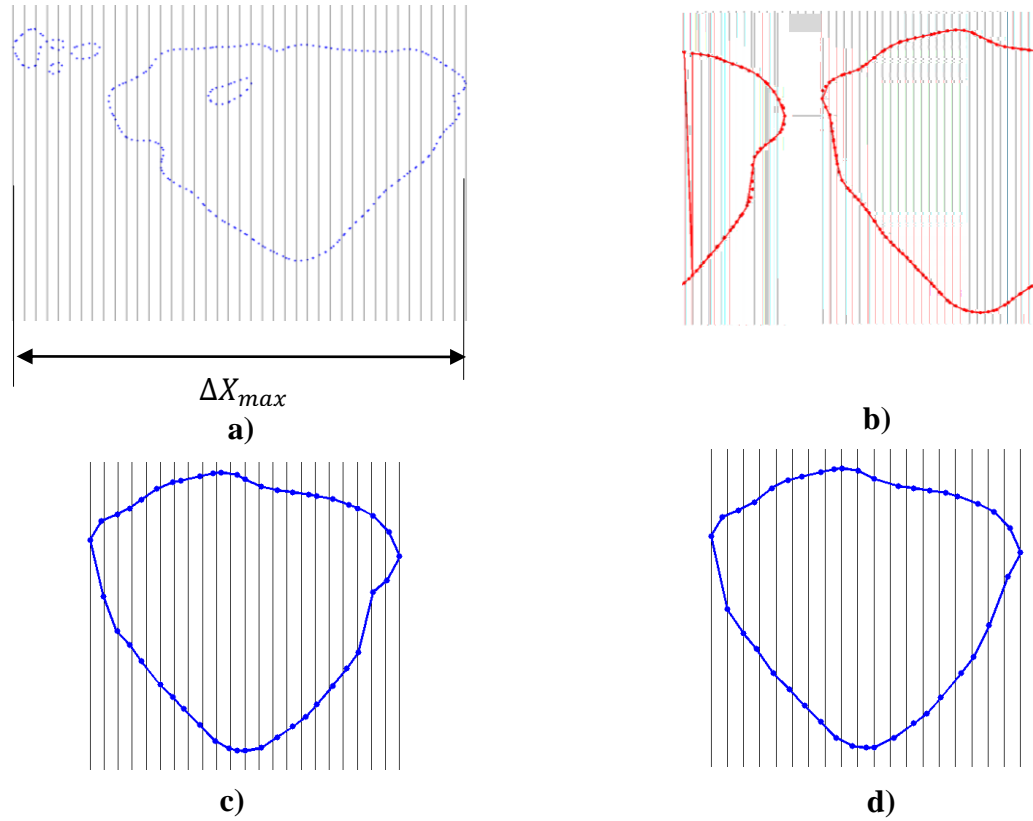
Figure 3.6: Determination of appropriate bin size: **a)** initial estimation of even-sized bins, **b)** erroneous inner contour determination for minimum two points/bin, **c)** corrected inner profile for minimum three points/bin, and **d)** extracted inner contour points for minimum four points/bin.

In the current approach, the only criterion used to control the size of the bins was the minimum number of points required in each bin. Heuristic searches performed with this technique on multiple humeral specimens have indicated that each bin should contain at least three points in it in order for this approach to work:

$$\text{count}_{\forall i \leq n_{\mathcal{B}}}(P) \geq 3 | P \in \mathcal{B}_i i \in \mathbb{N} \tag{3.3}$$

where the condition $P \in \mathcal{B}_i$ is equivalent to:

$$\min_{\mathfrak{B}_i}(X) \leq X_P \leq \max_{\mathfrak{B}_i}(X), \forall i \leq n_{\mathfrak{B}}, i \in \mathbb{N} \tag{3.4}$$

It is relatively easy to infer that the enforcement of the condition detailed in Eq. (3.3) generally leads to slight decreases in the number of bins as initially estimated with Eq. (3.4). However, as Figure 3.6b shows, a minimum number of two points in each bin does not represent a feasible option since unexpected jumps in inner contour might occur after the next processing steps are performed. By contrast, when minimum three points per bin are enforced, the inner contour is correctly detected (Figure 3.6c). Further increases of the minimum number of points per bin will also yield acceptable contours (Figure 3.6d), but points are more spaced apart and thus will capture less accurate details of the inner boundary.

The explanation of this phenomenon resides in the technique used to select inner contour points combined with their intrinsic density/spacing within the preprocessed data. Essentially, the determination of inner contour points relies on the identification of points that are characterized by maximum/minimum Y coordinates in each of the previously identified bins:

$$P_{I_c} = \left\{ P \in \mathcal{D} | Y_P = \max_{\mathfrak{B}_i}(Y) \text{ or } Y_P = \min_{\mathfrak{B}_i}(Y), \forall i \leq n_{\mathfrak{B}}, i \in \mathbb{N} \right\} \tag{3.5}$$

Once all points meeting this condition have been located (Figure 3.7a), the algorithm generates the inner canal contour simply by joining all points with identical attributes $(\max(Y), \min(Y))$ to be followed by final interconnections between the two categories mentioned that are always distinctively positioned either in the upper or the lower zone of the analyzed boundary (Figure 3.7b).

33

a)   **b)**
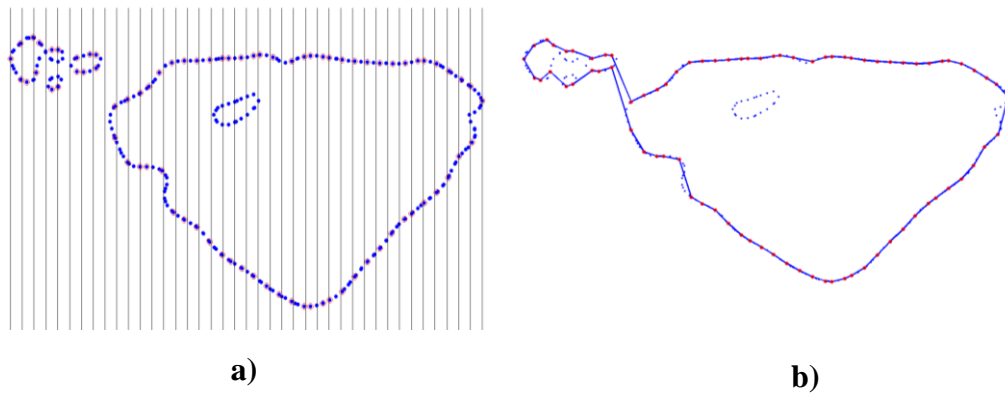
Figure 3.7: Determination of point-based inner contours: **a)** selection of contour points, and **b)** extracted final inner contour.

As a result of the technique used to select the vertices of the inner boundary, it becomes clear that if the bins are too small/narrow, it is possible that all (both) of its points will be incorrectly placed on the same upper/lower (*e.g.* anterior/posterior) region of the boundary, which in turn will translate into erroneous contours like the one shown in Figure 3.6c. Evidently, the conclusion to be drawn here is that the segmentation method used to generate the preprocessed data will ensure the required variation in point position only if at least three points/bin are enforced.

3.6   NUMERICAL RESULTS

The overlay of sample raw CT images with outer and inner bone contours extracted through the techniques detailed in sections 3.4 and 3.5 suggests that – in general – an adequate match exists between them. Clearly, the non-homogeneity of the cortical structure along with the geometric complexity of the endosteal canal still pose challenges when attempting to identify the three principal zones of the humeral cross section (Figure 3.8).
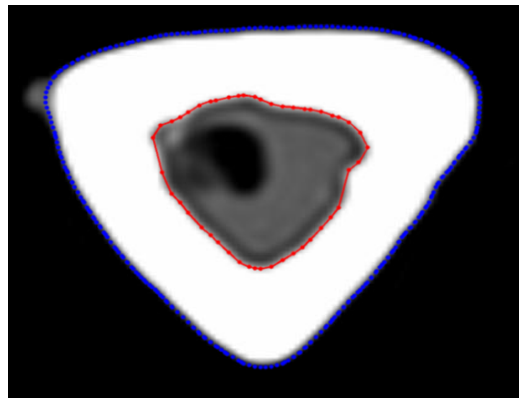
a)
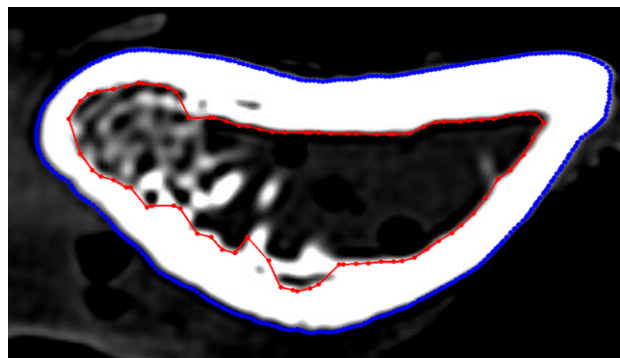
b)

c)

Figure 3.8: Sample overlays between raw CT slices and final extracted contours: **a)** superior match characteristic to medial zone of the humerus, **b)** approximated inner contours characteristic to distal humerus, and **c)** special/non-characteristic cases of inner canal configuration.

It is important to emphasize that while superior matches between CT and

extracted bone contours generally exist in the medial region of the humerus (Figure 3.8a),

special cases might also be occur as a result of particular cortical structure (Figure 3.8c). However, the local effect of inner contour "necking" will likely be minimal on the implant-bone interference amount since the stem is typically positioned centrally with respect to the endosteal canal in order to allow a good alignment between native and prosthetic FE axes. Similarly, the approximation of the inner canal walls that is characteristic to distal humerus, where cancellous/trabecular structure is more frequent, is not expected to confound much the interference results since most of the prominences are not captured by the extracted discrete contour. This is in fact in agreement with the experimental observation that most of the trabeculae tend to be crushed anyway during implant insertion procedure.

The application of the developed techniques for outer/inner contour extraction has resulted in specific point-based representations for each of the three analyzed humeral specimens (Figure 3.9). Although none of the conventional shading/rendering techniques that are currently available in CAD are capable to provide sufficient cues for an unambiguous visualization of the point datasets/clouds of points, a thorough examination of the three presented samples will reveal − at least in part − the anatomical variability that is inherent to many of the human skeletal components. In all three specimens, the distal zone of the bone was removed to preserve the similarity with the surgical procedure.
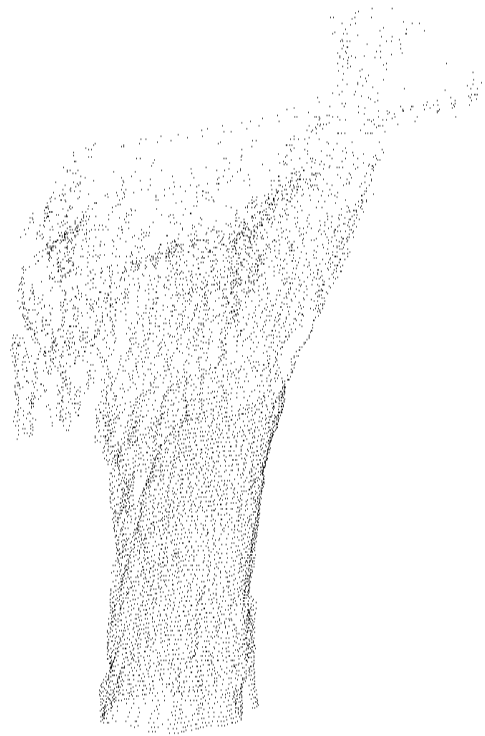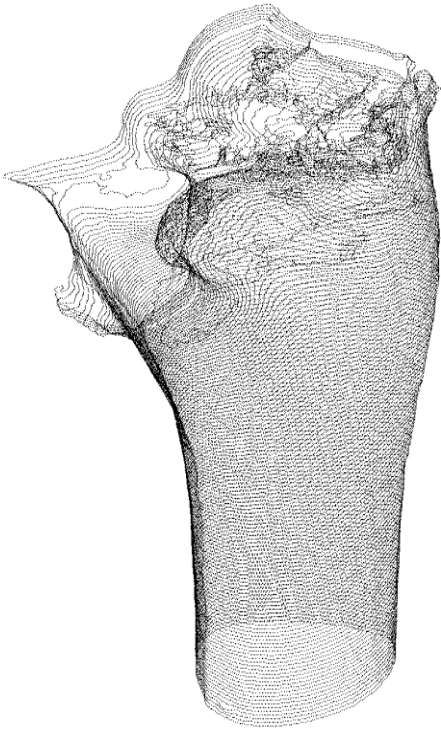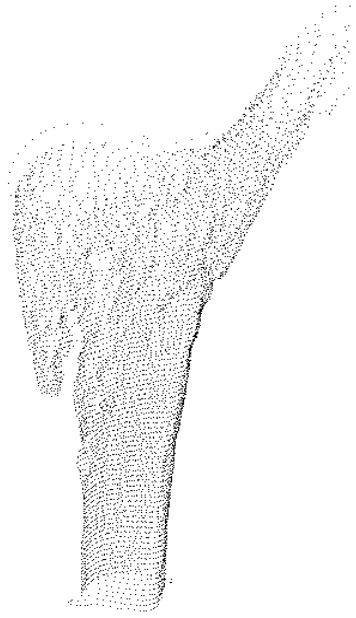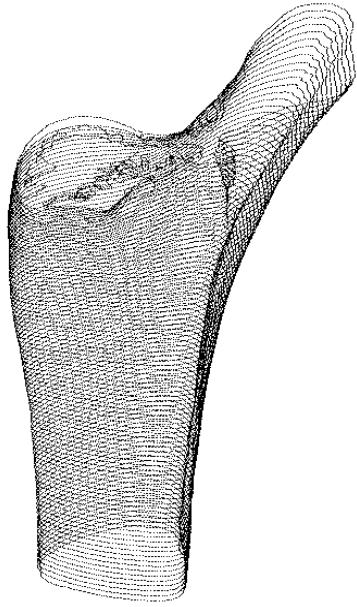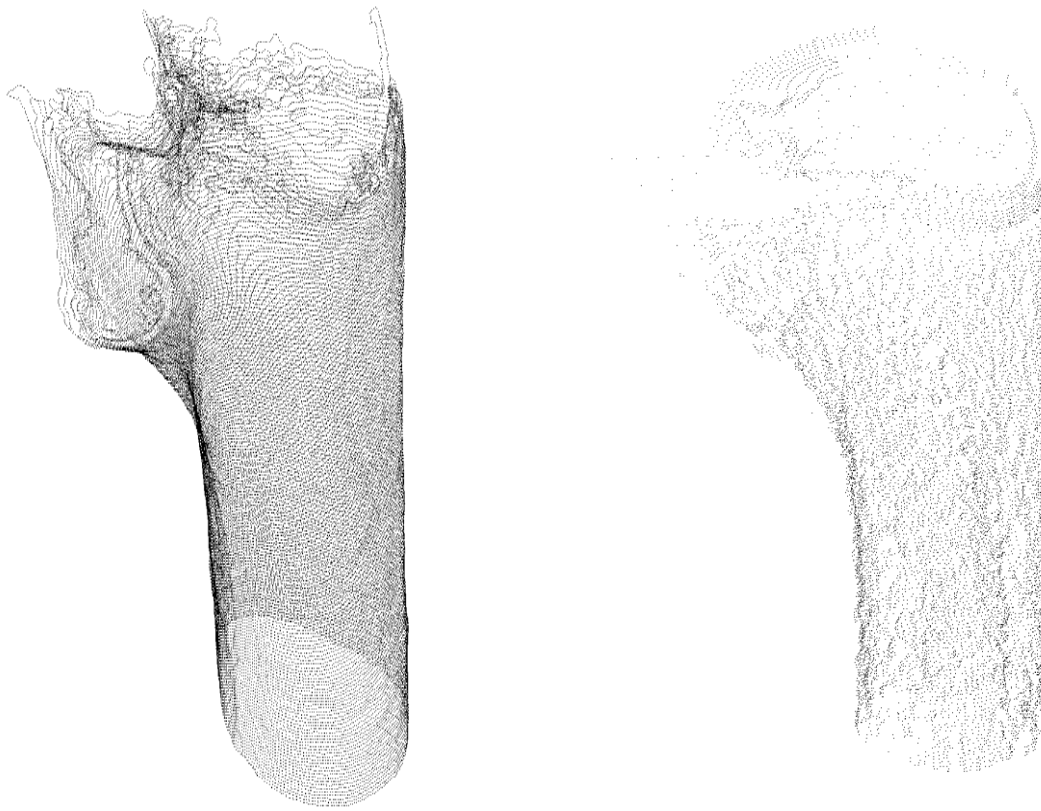
Figure 3.9: Final outer (left) and inner (right) contours for three different humeral specimens.

CHAPTER 4

MINIMIZATION OF THE INTERFERENCE BETWEEN HUMERAL IMPLANT AND BONE

4.1   OVERVIEW

The main goal of this chapter is to outline the numerical techniques developed in the context of the present study to minimize the amount of interference between the humeral stem and the cortical wall of the bone. As indicated in the previous chapters, the relatively large length of the humeral stem (anywhere between 40 and 60 mm) which is somewhat of a mandatory prerequisite for the appropriate fixation of the implant prevents – sometimes to a large extent – the successful alignment between the native and prosthetic FE axes of the elbow.

The biggest obstacle to overcome during the surgical procedure is represented by the unknown contact between the outer surface of the stem and the convoluted and uneven surface of the medullary canal of the humerus that is also characterized by a large geometric variability from one individual to the other. Since current preoperative protocols do not include appropriate tools for *a priori* determination/evaluation of the possible contact/interference zones, the surgeon is forced to make empirical, and thus prone to error, intraoperative decisions with respect to the location and amount of bone to be removed in order to ensure the best possible alignment between the two FE axes. Since the technology available today does not allow real-time visualizations of the bone removed during the surgical procedure, the surgeon performs cutting/machining operations without being able to predict their effect on the implant posture.

However, it is logical to postulate that the amount of bone to be removed should be minimized as much as possible both because this will preserve the best the inherent strength of the analyzed osseous component and because this will likely avoid its accidental penetration at all costs. As such, the preoperative assessment of a clinically acceptable implant posture that enables the aforementioned reductions in bone removal amount represents a viable objective to be pursued in the context of the present chapter.

4.2   PREVIOUS WORK IN IMPLANT OPTIMIZATION

Computer optimization algorithms assisting in the medical field is largely associated with image registration, segmentation techniques, computer aided diagnosis, treatment planning, and data mining tasks[56]. As a result, a limited amount of studies on the placement of prosthetic implants have been published. This is largely due to the fact that current limitations in the surgical procedure depend on the accuracy and repeatability of the surgeon's ability to place the implant into the desired target. With advances in computer assisted navigational techniques that increase both the repeatability and the accuracy of the implant placement, there will be a large need for computer algorithms to determine the optimal implant position. Currently, orthopaedic surgeons use visual cues or landmarks on the native bones in order to determine the placement of prosthetics. The following sections outline the work done in order to establish a repeatable optimization algorithm determining the optimal implant position for a distal humeral implant for total elbow arthroplasty surgeries.

4.3 MAXIMUM INTERFERENCE AMOUNT PER SLICE

For a certain position and orientation of the implant, the amount of interference between stem and humerus can be established based on their relative position. Once the geometry of the humerus is known, determination of the interference amount in each of its planar slices comes down to identification of the interference status for each of the implant points (*e.g.* non-interfering, interfering and penetration), to be followed by the calculation of the distance with respect to inner canal points, whenever necessary (*i.e.* interference/penetration is detected).
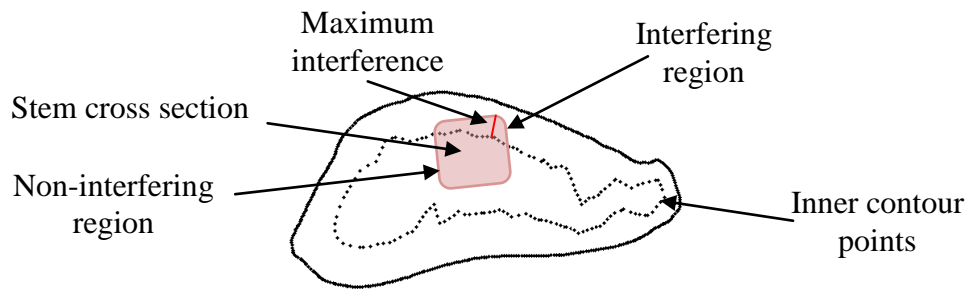
Figure 4.1: Determination of maximum interference amount in a planar slice.

4.4 DEFINITION OF THE IMPLANT POSTURE

Since the type of humeral implants used in the current study is characterized by a fairly simple shape of its stem whose shape is bounded by planar faces, its entire geometry can be described based on the location of 24 characteristic vertices $V_j^i(i, j \in \mathbb{N}, i \leq 3, j \leq 8,)$

located in three different planes: upper ($i = 1$), intermediate ($i = 2$) and lower ($i = 3$) (Figure 3.9a). Appropriate pairs of vertices V_j^i and V_j^{i+1} define the 16 characteristic edges $E_j^{i+1}(i, j \in \mathbb{N}, i \leq 3, j \leq 8,)$ that in turn delimit the 8 faces of the stem geometry.
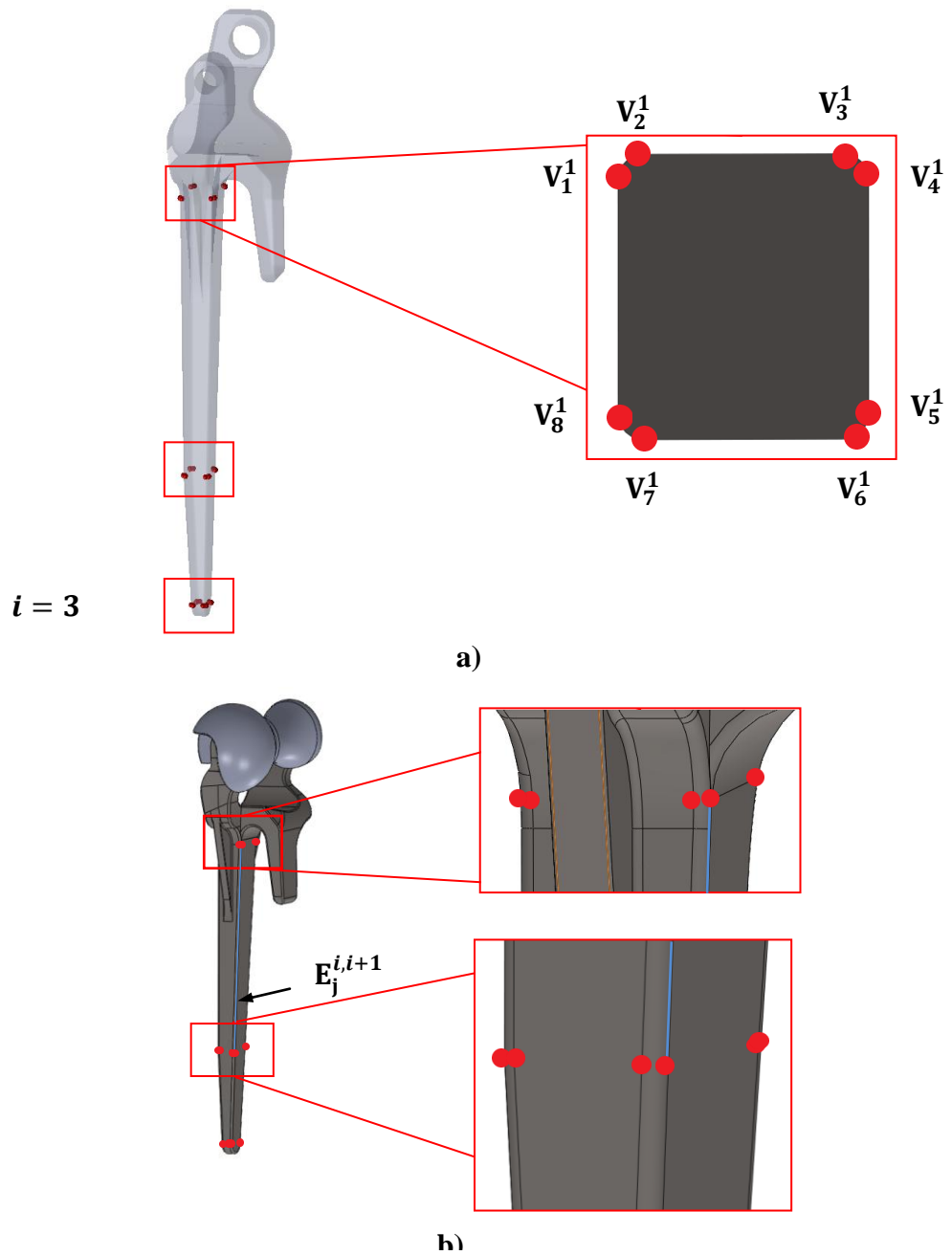
Figure 4.2: Significant geometric elements for implant stem: **a)** characteristic vertices, and **b)** characteristic edges.

Evidently, for a certain implant type, the geometric definition of the characteristic vertices and edges is preset and can be obtained through a direct interrogation of the solid

model. Furthermore, all points located along the characteristic edges can be determined with the known parametric relation:

$$\mathbf{P}_{E_j^{i,i+1}} = \mathbf{P}_{V_j^i} + u \cdot (\mathbf{P}_{V_j^{i+1}} - \mathbf{P}_{V_j^i}) \text{ with } u \in [0,1] \qquad (4.1)$$

It is important to emphasize here that all extracted vertex coordinates are dependent on two main parameters inherently associated with the aforementioned solid model, namely: the coordinate system and implant posture. In the context of the present study, implant posture ($\mathbf{\Omega}_I$) is defined as the 6D vector obtained through the concatenation of the 3D vectors of associated with its position ($\mathbf{P}_I$) and orientation ($\mathbf{O}_I$), since this information is sufficient to describe the general (*e.g.* combined translation and rotation) motion of a rigid body:

$$\mathbf{\Omega}_I = [\mathbf{P}_I \; \mathbf{O}_I] \qquad (4.2)$$

To enable precise determinations of the amount of interference per slice, all points of the implant stem had to be converted into the fixed humeral coordinate system (HCS), the one attached to the bone (Figure 4.3a). The axes of this coordinate system were established by the CT scanner and then kept throughout the subsequent data processing stages. In terms of the actual definitions, X_H and Y_H were contained within the planar slices, while Z_H direction was established by enforcing a certain degree of parallelism between main scanning direction and medullary canal. The origin of HCS was set in the capitellum center of the humerus. On the other hand, the implant data was provided with respect to its own implant coordinate system (ICS) as illustrated by Figure 4.3b. Similarly to HCS, the origin of ICS was set in the center of the prosthetic capitellum. The

superscript "orig" in the figure corresponds to the original orientation of the ICS, and it was later dropped once the correspondence between ICS and HCS was established. This transformation between the two coordinate systems was acquired by simply overlapping the two FE axes, a transformation performed by means of a rotation with α_{IH} angle about a vector $\hat{\mathbf{n}}_{\mathrm{IH}}$ ($\hat{\mathbf{n}}_{\mathrm{IH}} = \hat{\mathbf{n}}_{\mathrm{FE_I}}^{\mathrm{orig}} \times \hat{\mathbf{n}}_{\mathrm{FE_H}}$) as shown in Figure 4.3b. One of the results of this transformation is that the two FE axes will overlap ($\hat{\mathbf{n}}_{\mathrm{FE_I}} = \hat{\mathbf{n}}_{\mathrm{FE_H}}$)).
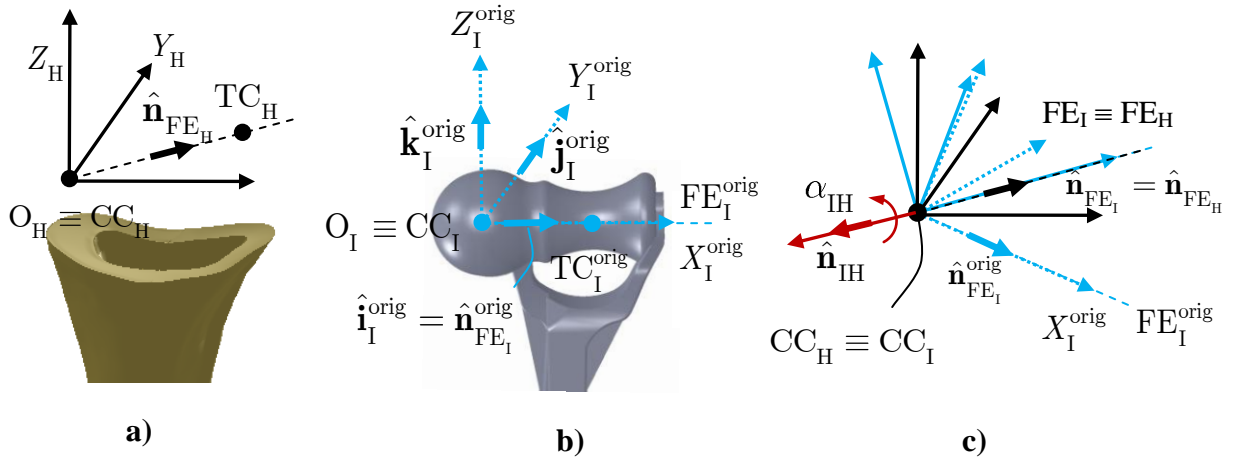
Figure 4.3: Coordinate transformation from implant to humeral coordinate system: a) humeral coordinate system, b) implant coordinate system, and c) rotation to overlap native and implant FE axes.

The rationale behind this particular type of coordinate transformation resides in the intent to simplify, as much as possible, the subsequent computational phases by enforcing the quantification of the implant posture with respect to an ideal case of perfect alignment between native and prosthetic FE axes. By doing this, all translational and rotational motions that are determinant for implant posture would represent nothing but direct measurements of the implant malalignment. However, since the standard clinical definition of the malalignment does not include rotation of the implant about the FE axis itself, the initial orientation of the implant was chosen to roughly follow the canal by

enforcing the parallelism between the longitudinal axis of the stem and a line determined by the centroids of two arbitrarily selected humeral slices. A more accurate determination of the initial stem orientation is not necessary because for the wide majority of bone-implant pairs the interference free conditions are not attainable anyway when FE axes are perfectly aligned. As such, no major differences would exist between the initial poses of the stem, to serve just as initialization parameters in the upcoming optimization algorithms.

Furthermore, to facilitate the clinical interpretation of the results, the modified implant posture was quantified directly in terms of malalignment between native and prosthetic FE axes, to translate in positional and angular variations (Figure 4.4). A total of six scalar components were used to characterize the instantaneous implant posture with respect to the initial pose – perfectly aligned FE axes.

$$\Omega_I = [X_{CC}\ Y_{CC}\ Z_{CC}\ \alpha_{FE}\ \alpha_{VV}\ \alpha_{IE}] \qquad (4.3)$$

In Eq. (4.3), X_{CC}, Y_{CC}, Z_{CC} are the three components of the translation between native (CC_H) and prosthetic (CC_I) centers of the capitellum and α_{FE}, α_{VV} and α_{IE} represent flexion-extension, varus-valgus and internal-extension angles, respectively. As Figure 4.4b-d indicates, the three rotations were defined with respect to the three axis of the ICS obtained after the α_{IH} rotation, as follows: FE rotation was defined about X_I (α_{FE} angle), VV rotation was defined about Y_I (α_{VV} angle) and IE rotation was defined about Y_I (α_{IE} angle).
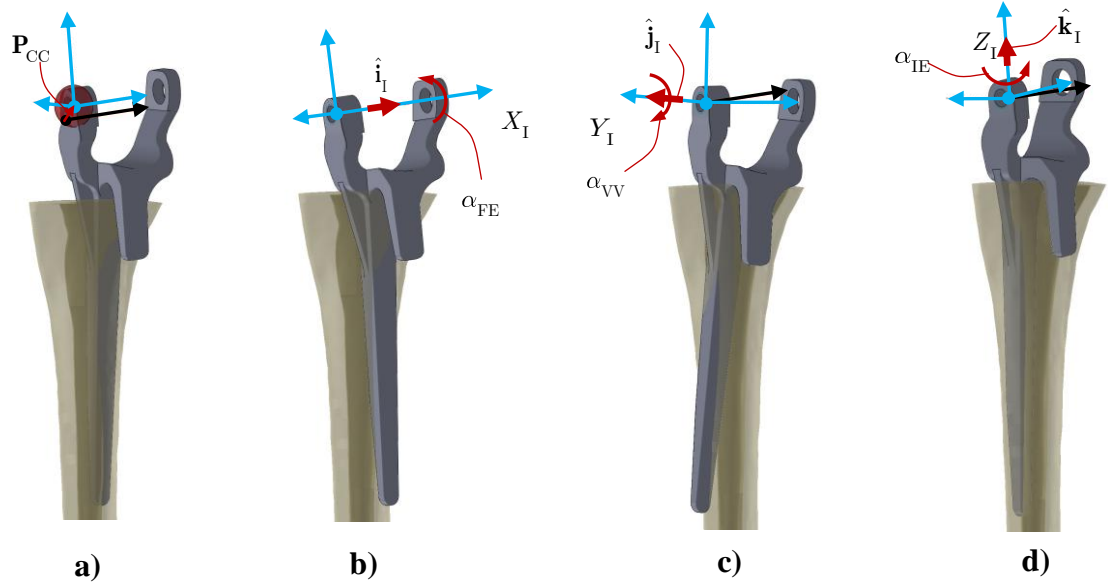
Figure 4.4: Characteristic elements of the implant posture: **a)** capitellar translation, **b)** flexion extension angle, **c)** varus-valgus angle, and **d)** internal-external angle.

As a result, the transformed (*e.g.* translated and/or rotated) posture of the implant can be expressed through standard homogeneous coordinate transformations controlled by the matrix:

$$\mathbf{T}_{\Omega_I} \ = \ \mathbf{R}_{\hat{k}_I}(\alpha_{IE}) \cdot \mathbf{R}_{\hat{j}_I}(\alpha_{FE}) \cdot T(\mathbf{P}_{CC}) \cdot \mathbf{R}_{\hat{n}_{IH}}(\alpha_{IH}) \tag{4.4}$$

The general coordinate transformation matrix $\mathbf{T}_{\Omega_I}$ enables calculation of the transformed position for any of the vertices of the implant as a function of the implant posture:

$$\mathbf{P}_V^{transformed} = \mathbf{T}_{\Omega_I} \cdot \mathbf{P}_V^{initial} \tag{4.5}$$

Here, the initial coordinates of the implant vertices $\mathbf{P}_V^{initial}$ were determined based on the aforementioned query of a specific implant model. Through recursive applications of Equation 4.5, the location of all 24 characteristic vertices of the implant can be determined as a function of implant posture. For detailed formulation of the coordinate

transformation matrices, the reader is referred to standard CAD/CAM textbooks, like for instance Zeid's book, Mastering CAD/CAM[57].

4.5 VARIATION OF THE IMPLANT POSTURE

When it comes to the determination of the optimal position in which the implant should be positioned inside of the humeral canal for implantation purposes, most orthopaedic surgeons will attempt to minimize the overall amount of cortical bone to be removed since this will diminish the long term durability of the prosthesis. From the perspective of the current work, the amount of bone to be removed is directly proportional with the global interference metric Δ outlined in Eq. (4.6). Since, as shown in Eqs. (4.6) and (4.7), the amount of interference per slice is dependent on the instantaneous position of the stem, it can be inferred that:

$$\Delta = \Delta(\Omega_I) \tag{4.6}$$

Eq. (4.6) quantifies the link between the total amount of interference and implant posture/malalignment. Based on this, the problem at hand is equivalent to determination of Δ_{min}, where:

$$\begin{cases} \Delta_{min} = \text{minimize}(\Delta) \\ 0 \leq |\mathbf{P}_{CC}| \leq d_{max} \\ \alpha_{FE_{min}} \leq \alpha_{FE} \leq \alpha_{FE_{max}} \\ \alpha_{VV_{min}} \leq \alpha_{VV} \leq \alpha_{VV_{max}} \\ \alpha_{IE_{min}} \leq \alpha_{IE} \leq \alpha_{IE_{min}} \end{cases} \tag{4.7}$$

As it can be noticed, the 3D translation vector was converted to a more concise magnitude constraint, primarily to preserve a higher clinical relevance of the results. For

practical implementation purposes, the three Cartesian components of $\mathbf{P}_{CC}$ were converted to spherical coordinates (r, θ, φ) that were also easier to constrain numerically.

According to Kim et al., in order to avoid complete implant wear, the varus-valgus malalignment angle should remain below 5 degrees. However, partial implant wear was shown to occur in the varus-valgus malalignment range of 3.5-5 degrees[13].

As Eq. (4.7) suggests, in order to determine the minimum interference amount, bounds have to be set for each of the six parameters encompassed by the implant posture. Since the surveyed medical literature has proved to be characterized by a relative paucity of information in this regard – most likely due to the technological complications associated with *in-vivo* measurements – somewhat arbitrary limits were chosen for each of the six variables, specifically:

$$\begin{cases} d_{max} = 5\text{mm} \\ \alpha_{FE_{min}} = \alpha_{VV_{min}} = \alpha_{IE_{min}} = -5° \\ \alpha_{FE_{max}} = \alpha_{VV_{max}} = \alpha_{IE_{min}} = 5° \end{cases} \qquad (4.8)$$

The primary rationale behind these numbers was to not exceed too much the range of feasible malalignment values characterized by rather small positional and angular errors.

The problem defined in Eq. (4.7) represents a classical problem of constrained nonlinear optimization for which an out-of-the-box gradient-based solver[59] was used since both objective and constraints – although highly nonlinear - were characterized by continuous first derivatives. To eliminate or at least diminish the relative confounding of the solution on the initial guess point, a global search solver was used on top of the local gradient-based one. In this regard, global search will run first the local solver from the

initial starting point. Once it converges, the global solver will estimate the radius of a

basin of attraction from the initial and converging point. A randomized initial set of trial

points within the constraints will be then generated and local solver will evaluate where

these set of points converge to. Once these points seems to converge reasonably well, a

comparative analysis is performed to determine whether the converged point is a local or

a global minimum in the test space[54,58,59,60,61].

In addition to global search, a "brute force" search technique was used to

determine the minimum interference amount, primarily for comparison and reference

purposes. Given the strong dependence of the optimization solution on the initial guess

value, a 6D array of initial guess points was dispersed in the posture space according to

scheme shown in Table 4.1. As mentioned previously, the $\mathbf{P}_{CC}$ translational distance

between the two capitella has been mapped into the spherical space for facilitate the

enforcement of clinically-relevant bounds. The graphical interpretation of the two angles

and distance used to define $\mathbf{P}_{CC}$ is provided in Figure 4.5.

Table 4.1 Grid of input parameters used for "brute force" search.

Input Parameter	Implant Position			Implant Orientation		
	r [mm]	θ [°]	φ [°]	α_{FE} [°]	α_{VV} [°]	α_{IE} [°]
Lower bound	0	0	-180	-5	-5	-5
Upper Bound	5	180	180	5	5	5
Increment	1	45	45	1	1	1
Total values	6	5	8	11	11	11
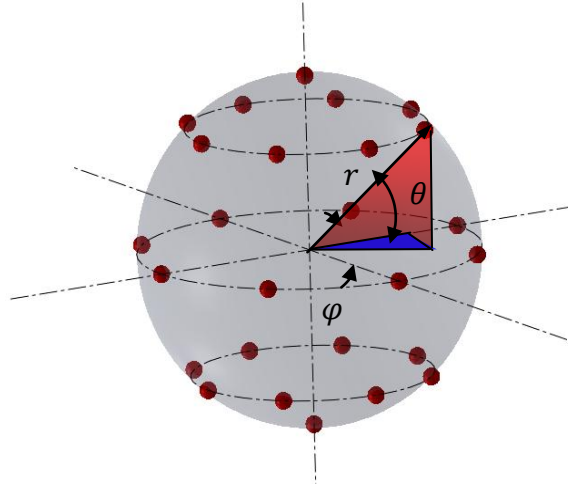
Figure 4.5: Discretized spherical coordinates of the 3D space used to quantify "cap-to-cap"

Since the total number of discretized guess points for each of the 6 spheres of variable radius (0,1,…,6) analyzed was 26 (= 8 x 3 + 2 poles), the total number of scenarios/initial guess points solved through the "brute force" approach yields at 207,636 (= 6 x 26 x 11 x 11 x 11).

4.6   MINIMIZATION OF THE INTERFERENCE AMOUNT

Since the position of the implant vertices and edges changes continuously as a function of the implant posture, it can be inferred that interference is also dependent on the six scalars outlined in Eq. (4.3). To quantify the total amount of interference between implant and bone (Δ), a metric has been defined as follows:

$$\Delta = \sum_{s=1}^{n_s} \delta_s \qquad (4.9)$$

where δ_S represents the maximum amount of interference existent in slice s while n_s is the number of slices in which interference is possible (stem length is smaller than that of the humerus).

For each of the bone slices located within the possible interference range ($s \in \mathbb{N}, s \leq n_s$), their intersection with 8 of the 16 characteristic edges of the implant was evaluated in order to determine the relative position of the implant cross section with respect to outer/inner contours of the analyzed slice. The calculation of the intersection points involves coupling of Eqs. (4.1), (4.4) and (4.5), such that:

$$\begin{cases} \mathbf{P}_E^{\text{transformed}} = \mathbf{T}_{\Omega_I} \cdot \mathbf{P}_E^{\text{initial}} \\ Z_S = d \end{cases} \qquad (4.10)$$

yields the coordinates of the 8 intersection points between the characteristic edges and the plane of the slice, S_S, positioned at distance, d, from the most distal one defined by $s = 1$ and $Z_S = 0$. Hence:

$$P_{S_j} = \left\{ P \in S_S | P = (E_j^{i,i+1})^{\text{transformed}} \cap S_s, i,j \in \mathbb{N}, i \leq 2, j \leq 8 \right\} \qquad (4.11)$$

which implies that $Z_{S_j} = d$. Once the intersection points per slice are known, the interference status for each of them can be determined based on well established algorithms capable to determine the relative position between a point and a polygon[62]. If the outer and inner contour polygons are denoted by $\mathcal{P}_{O_c}$ and $\mathcal{P}_{I_c}$ respectively then the maximum amount of interference per slice will be given by:

$$\delta_S = \max(|\mathbf{P}_{P_{S_j}} - \mathbf{P}_{P_{S_j}^C}|), j \in \mathbb{N}, j \leq 8 \qquad (4.12)$$

where $P_{S_j}^C \in \mathcal{I}_C$ represents the closest inner boundary point to P_{S_j}. As a supplementary condition to be met, P_{S_j} is a valid interference point only if $P_{S_j} \notin \mathcal{P}_{I_c}$. For practical implementation purposes, the same nearest neighbor technique described at Section 3.4 was used to determine $P_{S_j}^C$.

While from a rather theoretical standpoint it could be argued that the maximum interference per slice might also be attained for a point outside of the investigated subset (P_{S_j}) of implant/bone intersection, it is believed that due to the relative uniformity of the inner walls – especially in the narrower humeral cross sections (*e.g.* away from the distal end of the bone, see Figure 3.8a) thus with a larger probability of interference – maximum interference will occur almost always in one of the eight analyzed points P_{S_j}.

4.7   NUMERICAL RESULTS

A synthesis of the optimization results obtained through the two solving techniques is provided in Table 4.2. As expected, differences in terms of results are visible between the two solving techniques used. However, lower (better) interference values were obtained through global search which is most likely an indication that this method is more precise and thereby superior to "brute force", not only in terms of runtime, that is however, dramatically different as well. Of course, the high nonlinearity of the problem makes the attainment of identical (or close) results through both numerical solving approaches virtually impossible. However, although the results differ in terms of final objective function, a certain consistency can be noticed among final posture values, especially in the sense that in most scenarios the algorithm stopped because the bound for one of the input variables (generally the same) was reached through both solving

techniques. This could be regarded as a positive indication on the correctness and/or robustness of the approach.

Furthermore, since most of the bounds reached were angular, it can be inferred that for TEA, rotational malalignments seem to be more restrictive than the translational ones. While arguably some of the bounds could be loosened to achieve smaller interference values (like, for instance α_{FE} that does not have a direct impact on the malalignment), it can be noticed that the final "cap-to-cap" distances are already somewhere to the upper limit of the clinically acceptable range and therefore their further expansion might not be desirable.

Table 4.2: Summary of minimized interference and final implant posture results.

Sample No.	Optimization Algorithm	Implant Position			Implant Orientation			Δ_{min} [mm]	Solving Time [min]
		X_{CC} [mm]	Y_{CC} [mm]	Z_{CC} [mm]	α_{FE} [°]	α_{VV} [°]	α_{IE} [°]		
1	"Brute force"	0.00	0.00	5.00	-4.00	2.00	-1.00	50.96	1,260
	Global search	-1.68	-0.36	4.69	-5.00	0.33	-1.43	39.62	57
2	"Brute force"	-4.00	0.00	0.00	-5.00	2.00	-5.00	3.58	2,052
	Global search	-4.14	0.00	0.33	-5.00	1.82	-5.00	3.40	17
3	"Brute force"	1.50	-1.50	-2.12	-3.00	-5.00	-5.00	0.00	1,285
	Global search	0.52	-0.59	-0.66	-0.77	-5.00	-5.00	0.00	36

Interestingly, the three specimens tested suggest that the minimum interference free position can be reached in a variety of ways for each of the humeral specimens. These could involve: i) a primarily upward translational motion (essentially similar to implant extraction motion) for specimen 1 (definitely the one with the most challenging implantation/implant fit problem), ii) a primarily anterior/posterior translational motion combined with maximized angular variations for specimen 2, and iii) a minimal

translational motion combined with maximized angular malalignment. The values in Table 4.2 also indicate that a broad range of interference values could be encountered in clinical practice. The nil interference observed for specimen 3 simply means that an interference free posture was detected by the solver. However, whether the required implant malalignment that is required to attain the predicted minimum interference value is acceptable or not from a clinical perspective, it remains to be determined through more appropriate studies.

4.8   CLINICALLY RELEVANCE OF THE RESULTS

While all numerical results and comments presented in Section 4.7 have their own clinical implications, it is logical to postulate that orthopaedic surgeons would be
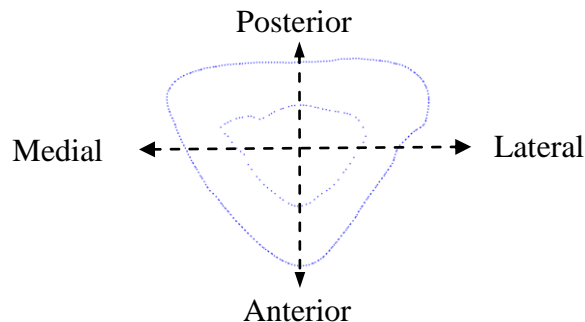
Figure 4.6: Principal anatomical directions with respect to cross section.

interested to know, prior to the actual surgical procedure, what are the areas of the humeral bone that are most likely to require cortical bone removal in order to allow implant insertion and fit. To enable further guidance on the anatomical location of the interference point, each humeral cross section was subdivided in four main regions according to the standard anatomical planes (Figure 4.6) and the common intersection point of the regions was assumed the centroid of each bone cross section.

To address more directly the clinical needs, Figure 4.7a outlines the amount of interference per slice (δ_S) as determined through the developed approach for humeral specimen 1 ("brute force" case). The slice index (s) runs in a distal to proximal direction, slice 1 corresponding to the plane used for osteotomy/excision of the distal humerus as shown in Figure 2.6b. The relative positioning of each slice in Cartesian coordinates can be determined based on the CT voxel size, which for in this case was set to 0.625 mm. As the graph suggests, the minimum interference position identified in Table 2 translates at slice level into a highly variable amount of interference per slice as well as a variable anatomical localization on the surface of the endosteal canal.

It is realistic to believe that the real amounts of bone to be removed might be different than those suggested by Figure 4.7a due to a variety of errors propagated in the process even from the early imaging phases. However, this type of information could serve at least as a qualitative guide to replace the current "blind" or "semi-blind" approach currently used in the surgical practice. Moreover, although the precision of the developed technique could be questioned with respect to the its physical counterpart, it is worth to be mentioned here that − even for the case with the largest Δ - the maximum amount of interference per slice was in the "interference" than "penetration" range, since the cortical thickness for the humerus was reported somewhere around 4.4 ± 1.0 mm[63] This observation validates − perhaps indirectly − that the proposed approach is feasible, or at least to a certain extent.

Virtually the same plot as in Figure 4.7a, but perhaps in a more suggestive three-dimensional representation is depicted by Figure 4.7b. For clarity of the figure purposes,

the scale of the maximum interference per slice was exaggerated and inner surface of the canal was represented in a surface form since point datasets are difficult to visualize.
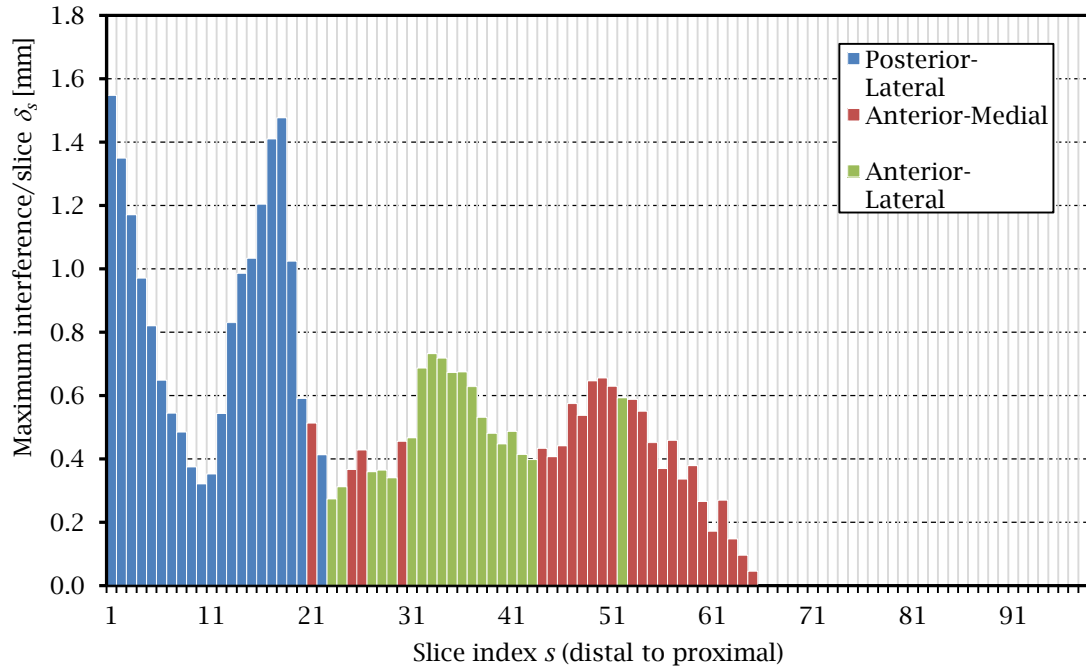
a)
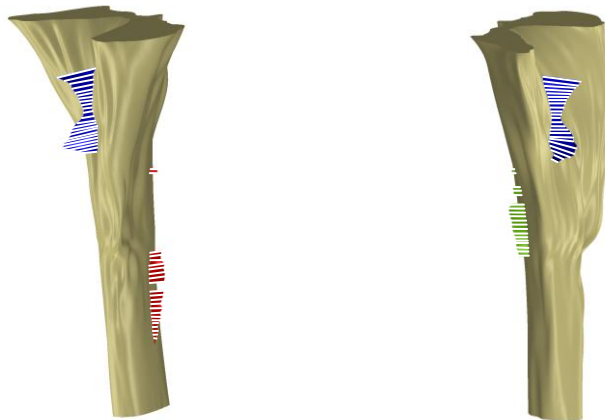
b)

Figure 4.7: Variation of the maximum interference amount per slice: **a)** numerical values and **b)** 3D positioning of the interference (exaggerated scale) with respect to inner canal surface for bone sample 1

CHAPTER 5

MINIMIZATION OF FLEXION-EXTENSION AXIS MALALIGNMENT AND INTERFERENCE

5.1   OVERVIEW

By contrast with the previous chapter which is focused on minimization of the bone removal amount through the variation of the implant posture within viable limits, the current section will treat both metrics as objective functions in an attempt to reduce to the maximum both implant/bone interference as well as implant malalignment. According to their established definitions, direct relationships exist between implant posture and its malalignment as well as between implant/bone interference and bone removal amount.

However, it is important to recognize that a relationship of inverse proportionality generally exists between implant malalignment and the amount of cortical bone to be removed from the medullary canal. Given the broad anatomical diversity of the humeral canal configuration, the strength of this inverse relationship is relatively low. Nevertheless, the general perception of those in the field is that larger endosteal canals would allow superior FE axes alignments and this will be further exploited to define a new research problem.

According to these observations, it becomes clear that simultaneous optimization of both metrics represents a common instance of a multiobjective problem, in which the decision with respect to optimal solution has to be made with respect to multiple – *i.e.* two in this particular case – often conflicting criteria.

Similar to most nontrivial multiobjective optimization problems, it is reasonable to believe that it is unlikely that a single optimal solution will be identified in this case[64]. In fact, due to the improbability to attain simultaneously optimal values for all objective functions, this class of problems is typically solved either by simply identifying the whole set of Pareto optimal solutions or by selecting a unique solution which satisfies subjective criteria of the human decision maker involved in the process[65].
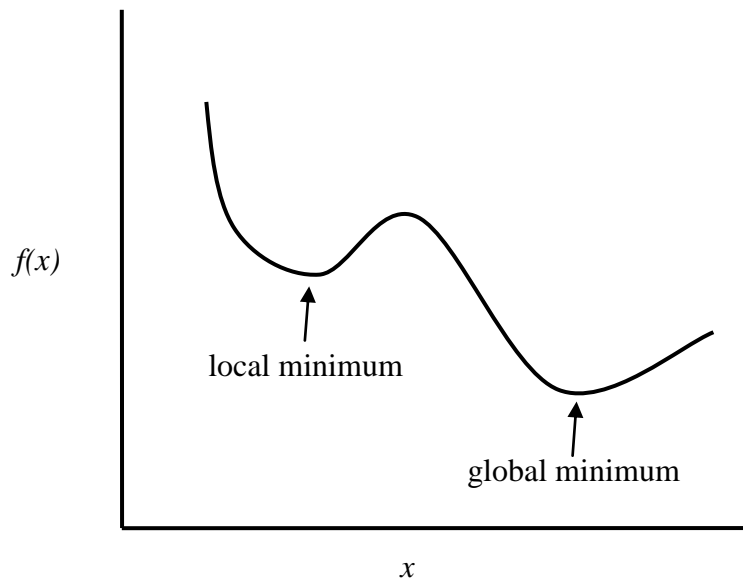
Figure 5.1: Two dimensional function with a local minimum and a global minimum.
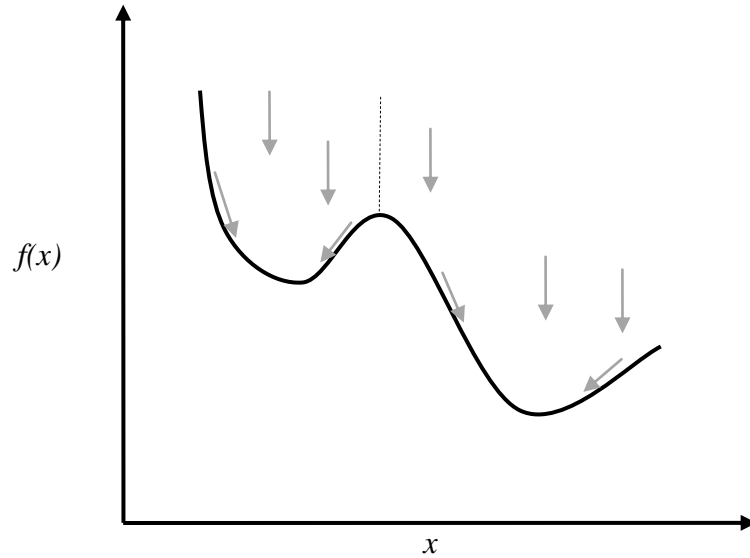
Figure 5.2: Two dimensional function with lines showing the direction of the gradient based search to arrive at the local minimums.

5.2 VOLUMETRIC DETERMINATION OF THE INTERFERENCE AMOUNT

To better quantify the amount of interference between the implant stem and the humeral cortical bone, an improved quantification metric was devised in an attempt to provide more accurate representations of the volume to be removed. Given the constant height of the CT voxels translated into equally spaced planar slices used in point-based representation of the bone, the first task to be solved is related to the quantification of the area of interference between implant stem and humerus.

To address this task, the polygonal shape of the implant stem was determined for each of the planar sections corresponding to the CT planes of the bone. For this purpose, the transformed position of the characteristic vertices of the implant (Figure 4.2) was initially computed through the application of the adequate coordinate transformations

required by the analyzed implant posture. Once the transformed position of the characteristic vertices were determined, the associated characteristic lines were intersected with CT scanning planes – known to be parallel to *XY* and determined by variable offsets along *Z* axis (Figure 5.3). Once the eight characteristic vertices of the stem were determined at the level of each relevant bone plane, the linear contour of the stem along with the inner bone boundary at the CT plane formed two polygons used in later calculations.
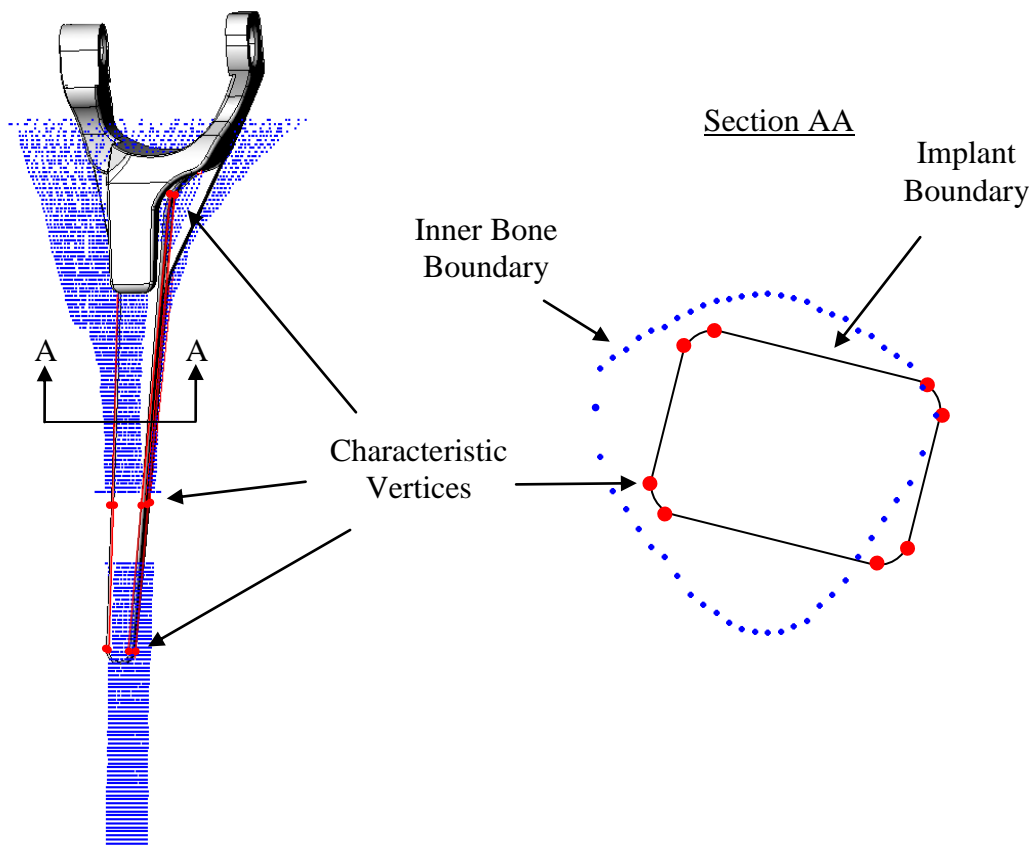
Figure 5.3: The generation of the implant stem boundary. Intersections of the CT cross sections with the characteristic lines along the implant stem corners generated the 8 implant points representing the corners of the implant stem for a given cross section.

Each planar section was then analyzed to determine the actual interference condition which can fall in one or more of the following three categories: i) non-interfering, ii) interfering, and penetration (Figure 5.4). This can be easily assessed based on the relative positioning of the implant points with respect to bone contours using an inpolygon function. If interference and/or penetration does exist, then standard functions for polygonal intersection were used to precisely identify the subset of stem vertices found in an interference/penetration condition. An outline of the numerical technique used to extract the polygonal intersecting between planar sections of the stem and bone is shown in Figure 5.7[66,67]. In a further investigation of how the polybool function worked, it was determined that after the polygons were ensured that they were closed and in a counter-clockwise form (CCW), the intersection points of the polygons were determined then the cross product of the intersecting vectors were determined. The result determined whether the contour was going inside the polygon or outside Figure 5.8.

a) Non-interfering   **b)** Interfering   **c)** Penetration
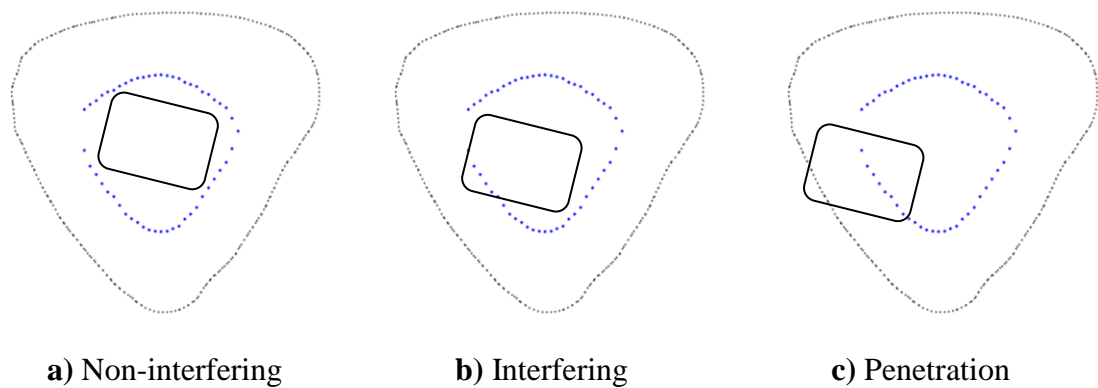
Figure 5.4: Three interfering categories of the implant stem.

In general terms, depending on purpose, several different types of Boolean operations are available to extract resulting polygonal regions (Figure 5.5). Since the

present work is exclusively concerned with determination of the stem area positioned *outside* of the inner bone contour, it becomes obvious that the only polygonal Boolean operation that can be used in this regard is Boolean subtraction.

Intersection

Union

Subtraction

Exclusive
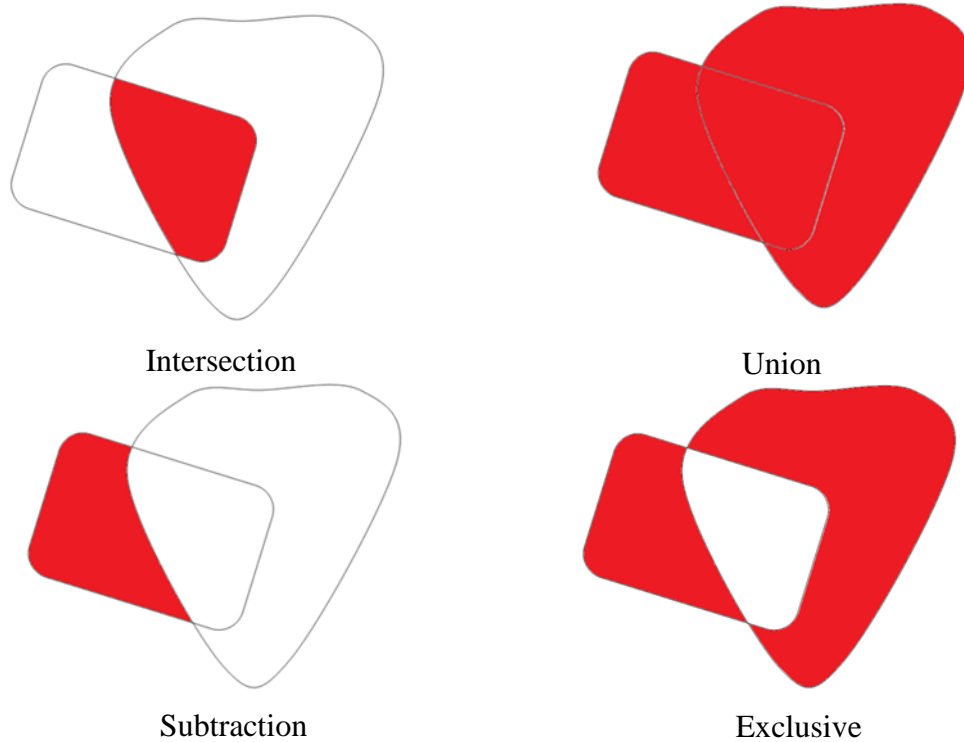
Figure 5.5: Boolean operations available for polygonal regions

In order to identify the intersection sections, intersecting points along the polygons were identified. If there were intersecting points, cross products of the vectors along the contours of the intersecting polygons were determined. The sign of the result determined whether the polygon was inside (interfering) or outside. In other words the cross product determined the start and ending points of the interfering polygonal sections. A visual representation of the vectors at the intersecting points can be seen in Figure 5.8.

Once the interfering subset of implant vertices was identified across the entire length of the stem (Figure 5.6), each of the planar areas of the interfering stem polygons have to be determined. While numerous techniques have been proposed in the past for polygonal area computations[68,69], the current study has relied on an implementation of the triangulation method[70]. In essence, the polygonal area is subdivided into sets of triangles. The areas of the triangles are easily computed and summated to arrive at the area of the polygon. Once individual interfering areas were determined, their summation was computed according to the algorithm presented in Figure 5.7.
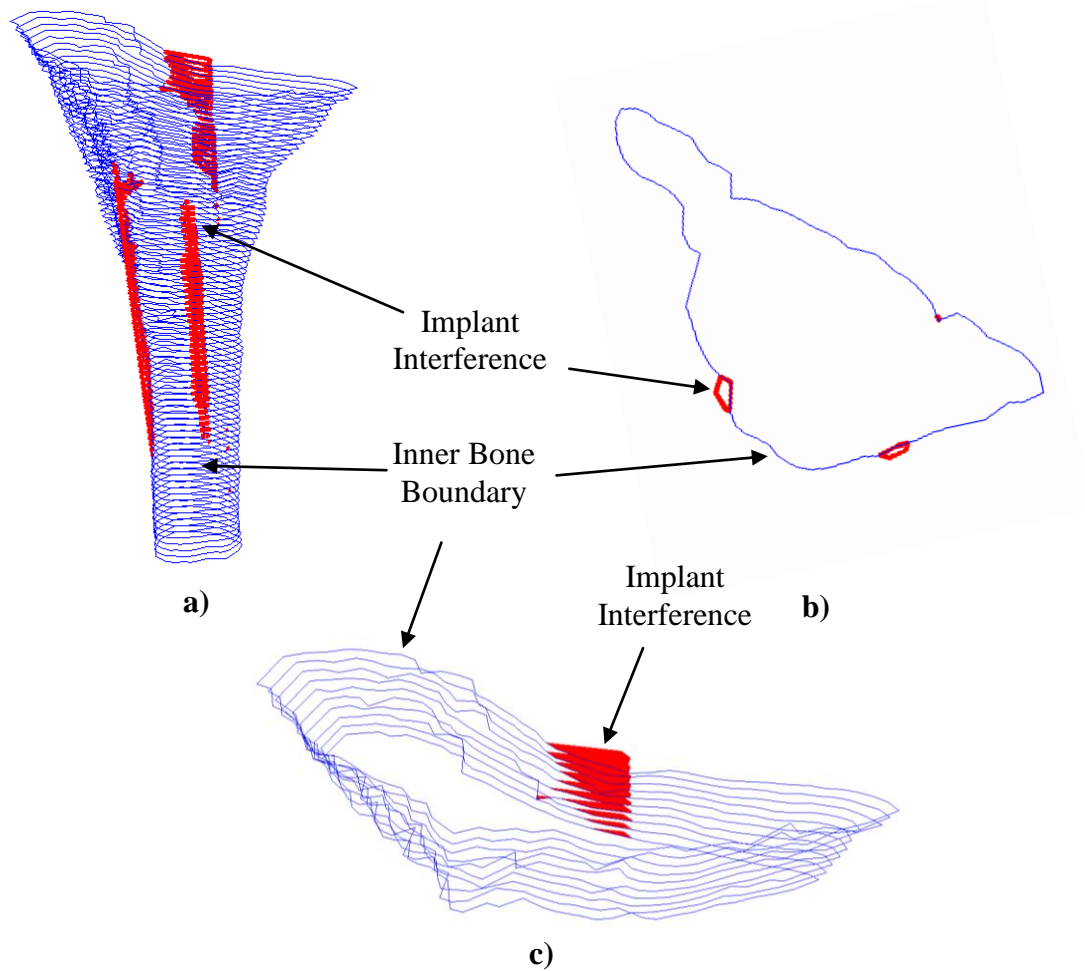
Figure 5.6: Interfering implant stem points with the inner bone canal. **a)** Entire 3D bone sample 1 implant interference. **b)** Zoomed in portion showing multiple implant interference areas. **c)** 10 distal CT layers showing the surfaces of interference.

63
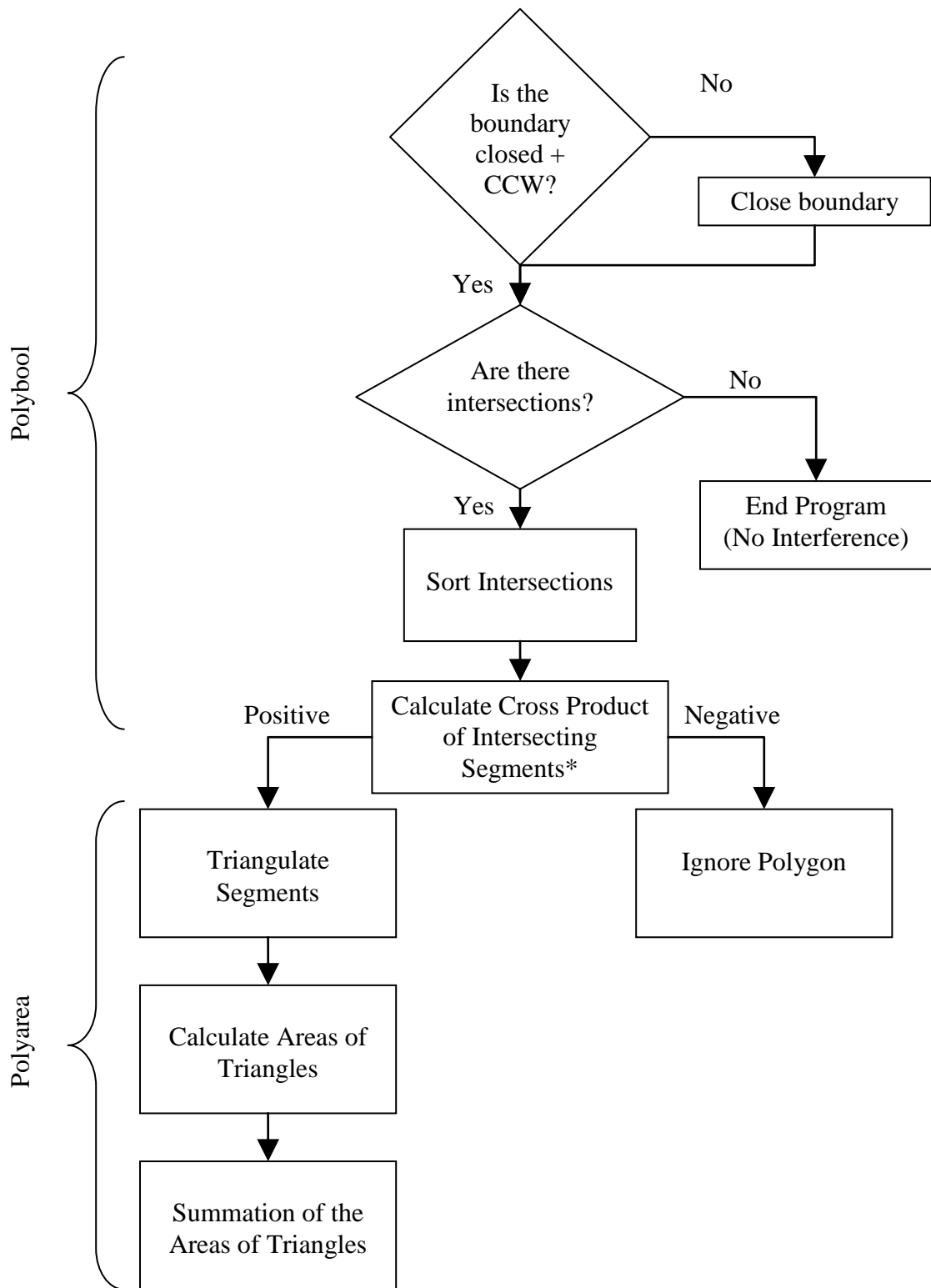
Figure 5.7: Flowchart of the Polybool and Polyarea functions.
*The cross product is taken to determine whether the contour of the intersection is going 'in' the polygon or 'out'.

It is important to note, though, that the sectional interfering area A_i^{int} calculated at the level of slice i is not necessarily formed from a single interfering polygon (Figure 5.8). Therefore, supplementary verification routines had to be used to determine the number of interfering polygonal "islands".
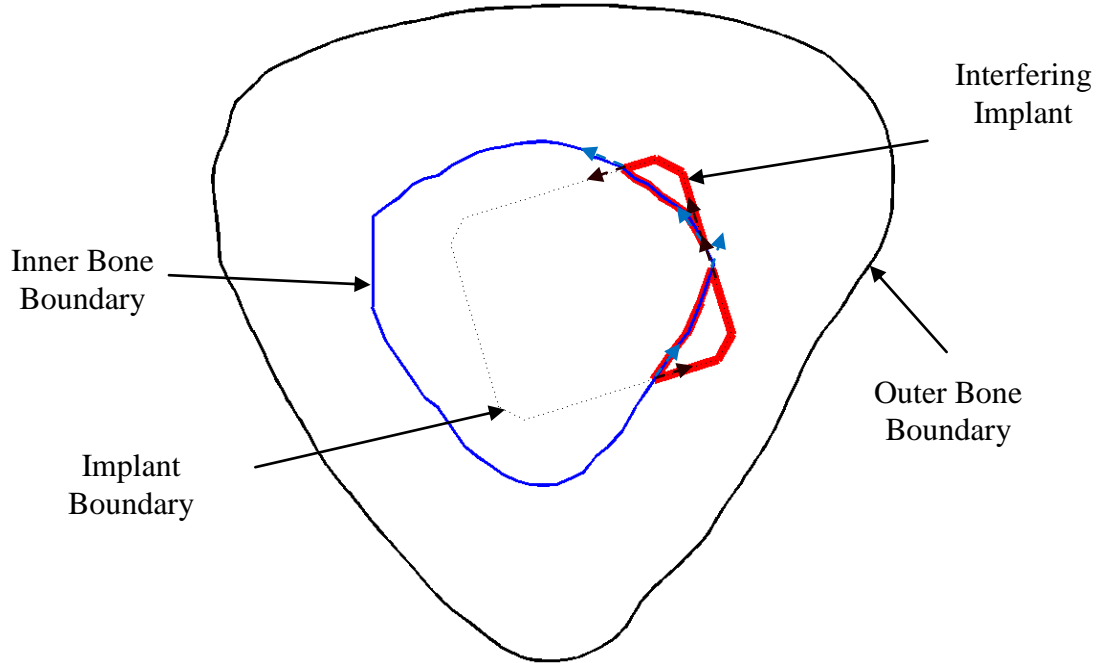
Figure 5.8: Interfering implant showing how the polybool and polyarea worked to quantify the amount of implant interference.

Once the cross sectional areas of interference were calculated, the sum of the area was evaluated and a volume of interference, V^{int}, could be estimated by multiplying the total area of implant interference, $\sum_{i=1}^{n} A_i^{int}$, by the distance in between each cross section, z_{CT} (0.625 mm).

$$V^{int} = \sum_{i=1}^{n} A_i^{int} \times z_{CT} \qquad (5.1)$$

A representative sample of volumetric interference amount computation is depicted in Figure 5.9a for bone sample 1 and implant posture determined by the following parameters (Table 5.1 page 77). For this particular implant posture, the fraction corresponding to the total interference amount was determined as being 2.57% from the total volume of the stem (3387025 mm^3). The overall variation of the volumetric amount across stem length is shown in Figure 5.9b.

a)   b)
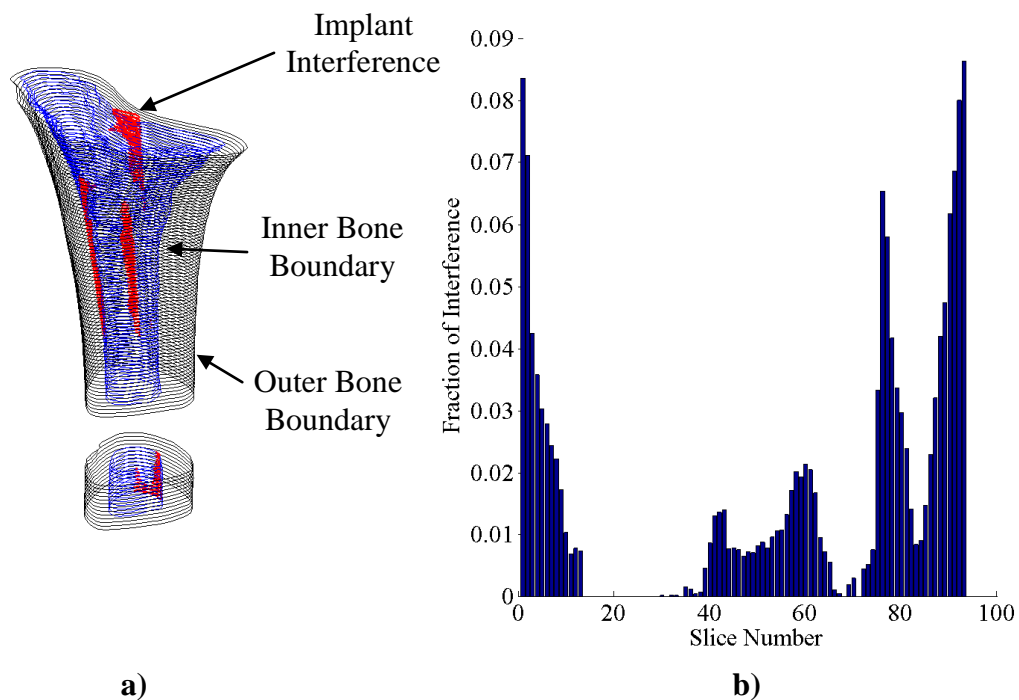
Figure 5.9: **a)** 3 dimension representation of the volumetric optimized implant position **b)** Bar plot showing the fraction of area of interference (A_i^{int}). The Slice numbers go from the distal to proximal position.

It is to be noted here that – from a theoretical standpoint – the volume of interference calculated through the point-based approach outlined above represents in fact one of the standard functions available in any of the commercial CAD systems based on conventional boundary representations (B-Rep) of the geometry (Figure 5.10). However, direct comparisons between the two approaches (*i.e.* point-based and parametric/B-Rep

66

geometries) were deemed difficult and thus not performed due to the approximations/errors introduced by the curve fitting algorithms required to convert the cloud of data points into a continuous surface-based format.
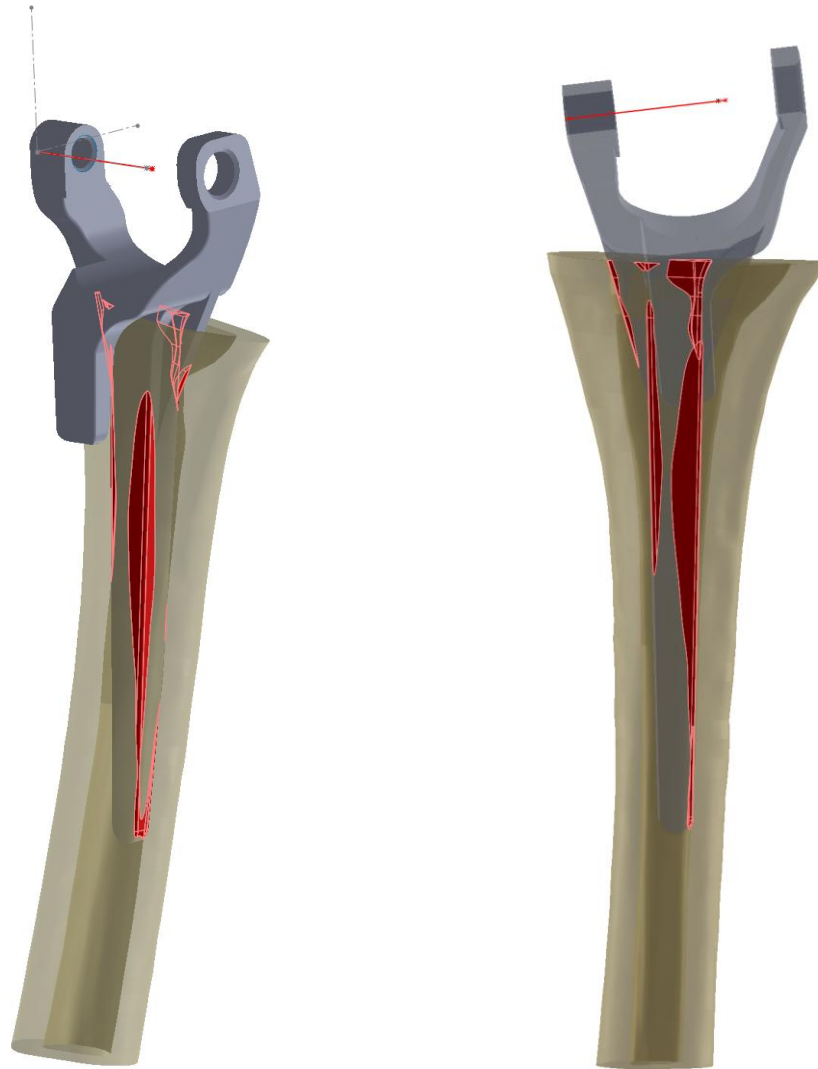
Figure 5.10: Rendered bone sample 1 with the interference shown using interference detection in Solidworks

5.3 DISTANCE TO THE OUTER BONE

Another metric considered was the minimum distance to the outer bone. This value is of concern as it is important to make sure there is sufficient bone stock left over so the orthopaedic surgeons would not compromise the bone strength when performing the procedure. During the bone reaming process, too much bone removal could compromise the strength of the bone leading to postoperative bone fractures. To address this, points were discretized along the boundary of the implant at each analyzed planar section. The minimum Euclidian distance from any one of the points on the implant to the outer bone boundary was recorded (Figure 5.11). This evaluation represented a 'worst case' scenario because the algorithm only considered the minimum distance to the outer bone. For each implant position, the CT cross section with the thinnest cortical bone portion was recorded along with the minimum distance to the inner bone boundary. The results are presented in the following section.
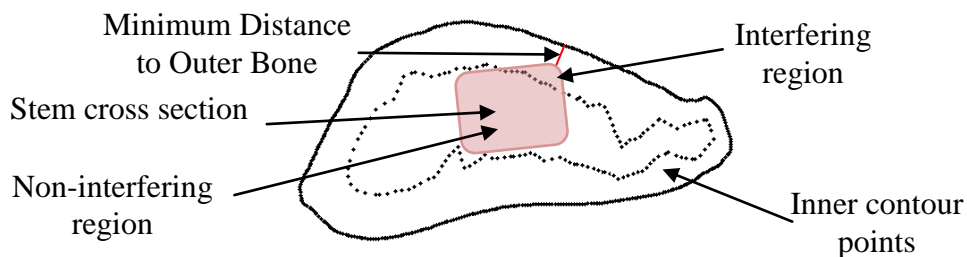
Figure 5.11: Determination of minimum distance to the outer bone in a planar slice.

5.3.1 Coefficient of Determination

In order to determine if the regression line accurately models the data points; it is common to calculate the coefficient of determination. The coefficient of determination is

the proportion of the total variability in the dependent variable that is accounted for by the regression line.

$$R^2 = \frac{SSR}{SST} = 1 - \frac{SSE}{SST}$$

where SST, SSR, and SSE are the total sum of squares, the regression sum of squares, and the error sum of squares.

$$SST = \sum_{i=1}^{n}(y_i - \bar{y})^2 \tag{5.2}$$

$$SSR = \sum_{i=1}^{n}(\hat{y}_i - \bar{y})^2 \tag{5.3}$$

$$SSE = \sum_{i=1}^{n}(y_i - \hat{y}_i)^2 \tag{5.4}$$

where y_i is the function value of the data point, $\bar{y}$ is the mean of the function values, and $\hat{y}_i$ is the expected values of the data based on the regression line. Another way to determine the total sum of squares is multiplying the number of observations, n, minus 1 by the variance, σ^2.

$$SST = (n - 1) \cdot \sigma^2 \tag{5.5}$$

From the normal of residuals $(y_i - \hat{y}_i)$, the mean $(\bar{y})$ and the standard deviation (σ) the coefficient of determination, SST and SSE can be calculated from formulas 25 and 24.

5.4 GENETIC ALGORITHM

Genetic Algorithm is an alternative solver to GlobalSearch and MultiStart. John Holland, the originator of the genetic algorithm first proposed his method in 1975[71]. It

wasn't until the late 1989 when the development of computers allowed the application of this algorithm.

During the initialization stage, an initial set of solutions, called a population, is either generated randomly or seeded in area where a solution is likely to be found. Individual solutions can also be called chromosomes. During successive generations, a portion of the initial population gets carried over into the next generation depending on their fitness values – more fit solutions are more likely to be passed on to the next generation. During the reproduction stage of the genetic algorithm, selected parent chromosomes pair up and form another set of potential solutions called children[64]. The children can either share different characteristics of the parent solutions, called crossovers, or make changes from a single parent, called mutations[59]. The fitness values of the child solutions are evaluated then a new generation is formed. This generally results in a higher fitness value and stops when the fitness value converges at the highest value or if other stopping conditions are met. Other stopping criteria include: a fixed number of generations met, a minimum criteria met, or a manual inspection. A pseudo code flowchart showing the genetic algorithm process can be shown in Figure 5.12.
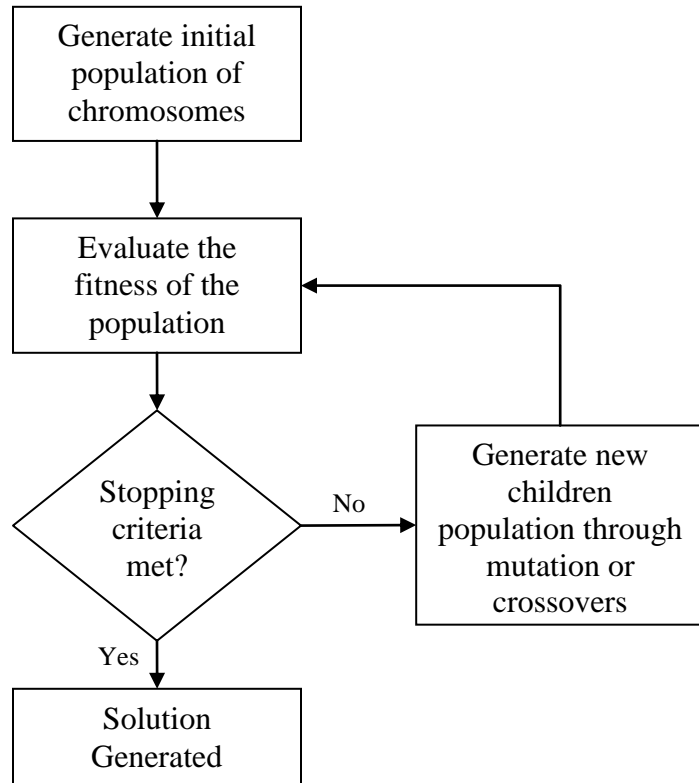
Figure 5.12: Flowchart of the genetic algorithm pseudo code.

A major benefit of the genetic algorithm is the computation time compared to

GlobalSearch and MultiStart. Another benefit of the genetic algorithm is the robustness

of the method. Since the algorithm does not require gradient information, the objective

functions and constraints are not restricted. Other benefits of genetic algorithm are that it

can run in parallel enabling the process to significantly speed up provided that there are

multiple cores available on a computer processing unit (CPU) to utilize. However, the

work done in this thesis did not use the parallelization techniques offered by the genetic

algorithm. Conversely, the genetic algorithm does not have a proof of convergence. As a

result, the solution generated may not necessarily be the optimal solution, but it is often close.

5.5   NORMALIZING MALALIGNMENT AND INTERFERENCE AMOUNT

In order to compare two objective functions amongst one another, it is important to ensure that the objective function values are at least in the same order of magnitude. Normalization of the amount of malalignment between the bone and implant flexion-extension axes and the normalization of the interference amount had to be evaluated. Once evaluated, the two could be compared amongst one another and an appropriate trade off value could be established arriving at an optimal solution to the implant posture.

Normalizing the malalignment amount was done based on the limits of the implant movement. Allowable implant movements were as follows;

$$
\begin{cases}
d_{max} = 5mm \\
\alpha_{FE_{min}} = \alpha_{VV_{min}} = \alpha_{IE_{min}} = -5° \\
\alpha_{FE_{max}} = \alpha_{VV_{max}} = \alpha_{IE_{min}} = 5°
\end{cases} \tag{5.6}
$$

Therefore, the following calculations were done to normalize the amount of malalignment from the native flexion extension axis;

$$
f_{mal} = \frac{\dfrac{\sqrt{(x^2+y^2+z^2)}}{d_{max}} + \dfrac{|\alpha_{VV}|}{\alpha_{VV_{max}}} + \dfrac{|\alpha_{IE}|}{\alpha_{IE_{max}}}}{3} \tag{5.7}
$$

$$
f_{mal} = \frac{\dfrac{d}{d_{max}} + \dfrac{|\alpha_{VV}|}{\alpha_{VV_{max}}} + \dfrac{|\alpha_{IE}|}{\alpha_{IE_{max}}}}{3} \tag{5.8}
$$

Flexion-extension angle, α_{VV}, was not considered in the amount of malalignment since a change in the flexion-extension angle of the implant did not affect the deviation amount from the flexion extension axes of the implant and bone. The sums of the normalized malalignments were divided by 3 to ensure that the objective function remains below 1. Since the max value of each individual parameter could be 1, the summation could be at a maximum 3.

Volume of interference could be represented as a fraction of implant interference by normalizing it by the total volume of the implant stem, V^{imp}. To calculate the total volume of the implant stem, a similar approach was used. Since the implant cross sections had already been identified at each planar CT section, the area of implant cross section, A_i^{imp}, was calculated using a polyarea function. Again, the summation of these areas multiplied by the thickness between each CT plane, z_{CT}, was a reasonable approximation of the implant volume. The following formulae show how the volume fraction of interference was calculated.

$$Interfering\ Implant\ volume\ fraction = \frac{V^{int}}{V^{imp}} \qquad (5.9)$$

$$Interfering\ Implant\ volume\ fraction = \frac{\sum_{i=1}^{n} A_i^{int} \times z_{CT}}{\sum_{i=1}^{n} A_i^{imp} \times z_{CT}}$$

$$Interfering\ Implant\ volume\ fraction = \frac{\sum_{i=1}^{n} A_i^{int} \times \cancel{z_{CT}}}{\sum_{i=1}^{n} A_i^{imp} \times \cancel{z_{CT}}}$$

$$Interfering\ Implant\ volume\ fraction = \frac{\sum_{i=1}^{n} A_i^{int}}{\sum_{i=1}^{n} A_i^{imp}} \qquad (5.10)$$

5.6   MULTIOBJECTIVE OPTIMIZATION

If there are multiple design objectives to consider, a multiobjective optimization technique approach is used to evaluate Pareto fronts for the multiple objectives. In other words, tradeoffs can be established in order to determine the appropriate weights of the respective objectives. In order to equally compare one objective, $f_1(x)$, to the other, $f_2(x)$, often the objective values are normalized causing the objective values to range from 0 to 1. Then, weights, w, can be established on each normalized objective function if the user believes one objective is more important than another. Once the objectives have been normalized and weights established, the multiple objectives combine into one single objective, $f_{MO}(w, x)$.

$$f_{MO}(w, x) \ = \ w \times f_1(x) \ + \ (1 - w) \ \times \ f_2(x) \hspace{2cm} (5.11)$$

Pareto curves are a representation of candidate optimal solutions based upon the evaluation on one objective function of another. The shape of a typical Pareto curve depends on whether or not the user is minimizing or maximizing the objective functions. The shapes of the four possible Pareto curves for two objectives are shown in Figure 5.13. For the purpose of this thesis, since the aim is to minimize the amount of interference and minimize the amount of malalignment, the first Pareto graph is applicable to the optimal implant position. An ideal optimal solution lies on the boundary of the Pareto curve and the selected solution depends on the importance of the objective functions.
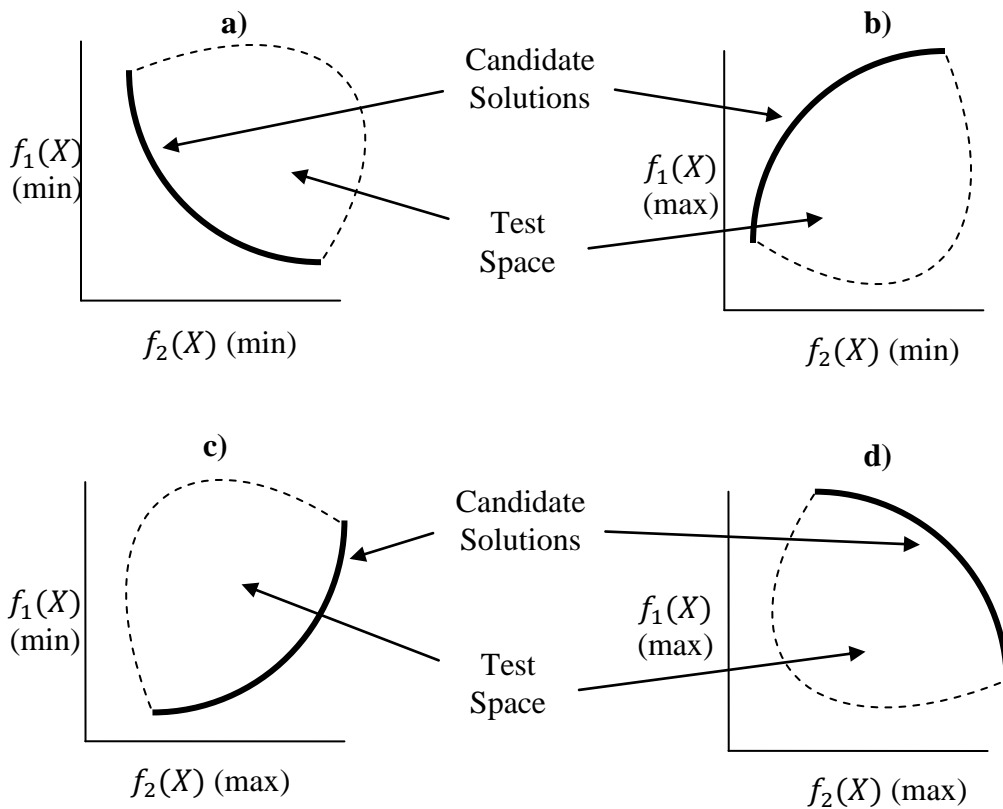
Figure 5.13: Typical Pareto curves for various double objective optimization problems. a) Pareto curve for minimizing both objective functions. b) Pareto curve for maximizing one and minimizing the other objective function c) Pareto curve for minimizing one and maximizing the other objective function d) Pareto curve for maximizing both objective functions.

Another way to determine an optimal solution is to assess weight functions amongst the objective functions made. This method is only suitable if the user initially knows how to relatively weigh the objective functions amongst each other. In other words, how important one specific objective is to other objectives. For this particular case, a weight, w, was assigned to the malalignment function, $f_{mal}(X)$, whereas the interference function, $f_{int}(X)$ was multiplied by the proportional weight, $1 - w$.

$$min(w \times f_{mal}(X) + (1 - w) \times f_{int}(X)) \tag{5.12}$$

where $0 \leq w \leq 1$ and X represents the implant posture.

When combining two or more objective functions with one another, it is also important to have the two objective function values within the same order. If they are not in the same order, one objective function is going to be weighted more heavily than the other even with assigned weights. For example, if one objective value function is 0.01 and the other is 10, the minimization algorithm will try to minimize the objective function value of greater value since it will have more of an effect of the minimization of the combined objective function.

In order to equate the two objective value functions with one another $f_{mal}(X)$, , was divided by 10 since typical volume of interference values were 0.01 - 0.1. Typical values for $f_{int}(X)$ were in the ranges of 0.1-1.

5.7   RESULTS

Table 3 shows the results done on 3 bone samples. Results of the "brute force" point and the global point search were from chapter 4 and are used to compare and validate the volume search method described in section 5.4. Genetic Algorithm was evaluated on each bone sample. The grey background in the Δ_{min} column represent how the interference was evaluated; either by maximum point of interference at each layer or the volume of interference. It is also important to note that the point based search is a summation of the distance to the maximum interfering point whereas the volume of interference is a percent of interference.

Table 5.1: Results comparing the maximum point of interference to the volume of interference

Sample No.	Optimization Algorithm	Implant Position			Implant Orientation			Δ_{min} [mm]	Δ_{min} [% Volume]
		X_{CC} [mm]	Y_{CC} [mm]	Z_{CC} [mm]	α_{FE} [°]	α_{VV} [°]	α_{IE} [°]		
1	"Brute force" point	0.00	0.00	5.00	-1.00	2.00	-4.00	50.96	3.84
	Global point search	-1.68	-0.36	4.69	-1.43	0.33	-5.00	39.62	2.60
	"Brute force" volume	-2.12	0	2.12	-1	0	-3	-	3.09
	Global volume search	-0.68	-1.85	4.60	1.50	0.19	0.61	-	2.57
	Genetic algorithm	-0.87	0.75	-1.28	-0.35	0.915	-1.02	-	3.57
2	"Brute force" point	-4.00	0.00	0.00	-5.00	2.00	-5.00	3.58	0.38
	Global point search	-3.99	0.00	-0.33	-5.00	1.82	-5.00	3.40	0.31
	"Brute Force" volume	-3.54	0	-3.54	-5	3	-5	-	0.25
	Global volume search	-4.04	0.049	-1.38	-4.99	2.24	-5.00	-	0.25
	Genetic algorithm	-2.34	-0.70	-2.59	-1.58	4.16	-2.42	-	0.86
3	"Brute force"	1.50	-1.50	-2.12	-3.00	-5.00	-5.00	0.00	0.0345
	Global point search	0.52	-0.59	-0.66	-0.77	-5.00	-5.00	0.00	0.0252
	"Brute Force" volume	2	-2	-2.83	-5	-5	-5	-	0.037
	Global volume search	0.12	-0.08	-0.21	-4.40	-4.83	2.30	-	0.037
	Genetic algorithm	0.062	0.000	0.67	-3.87	-4.84	3.65	-	0.0669

From Table 5.1, one can realize that all of the optimized positions converged at a similar implant posture. However, there was a noticeable difference in the time required for each algorithm and the amount of bone interference from each result. Namely, the genetic algorithm converged at a solution quickly but not necessarily fully optimized

since it generally resulted in an implant position with a greater amount of interference compared to the global volume search approach. Depending on whether time is a priority, the doctor could decide which method best satisfies his/her needs. For example, if the surgeon believes that the genetic algorithm presents a solution that is accurate enough, they could choose that for time saving purposes.

Clinically, not only do these results provide a target for surgeons to assist them in properly fitting the implant in the bone canal, these results can be presented to orthopaedic surgeons to assist them to find where exactly these interfering areas are located. From the illustrations in Figure 5.14, the orthopaedic surgeon will have a better understanding of where the bone should be reamed pre-operatively. Moreover, these results could be integrated with navigational assisted surgeries to ensure that the bone reamers/rasps/broaches are making contact in the appropriate areas of the cortical bone. Evidently, these representations provide the doctors more of an idea of the implant stem interference than the illustrations provided in Figure 5.14.
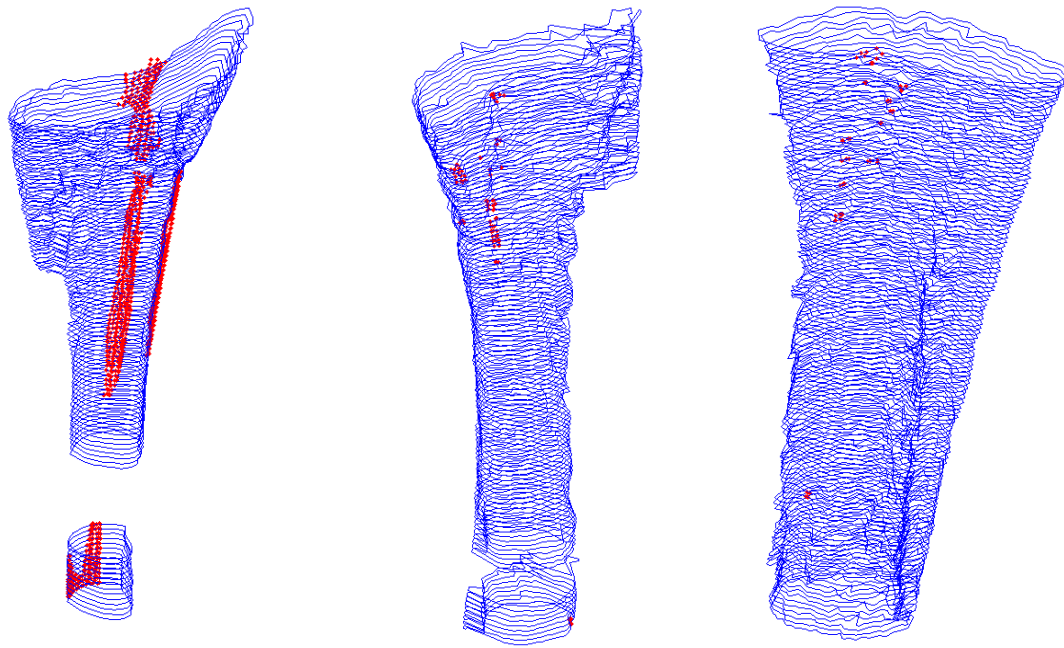
Figure 5.14: Three dimensional global volume search results on the three bone samples. The blue areas represent the inner bone boundary and the red points are of the implant stem boundary.

The results on evaluating the maximum distance to the inner bone boundary and the maximum distance to the outer bone are graphed in Figure 5.15-Figure 5.17. A maximum distance to the inner bone boundary represented a worst case scenario in terms of implant interference. If the surgeon were to remove the interfering bone, a thin section of cortical bone would remain. Similarly, the maximum distance to the outer bone represented a worst case scenario where the implant interfered with the bone the most. A negative distance represents that the point was inside the closed boundary where a positive distance is outside. Each blue dot represents an implant position and the implant was varied in the allowable discretized space in the same way as the brute force approach.
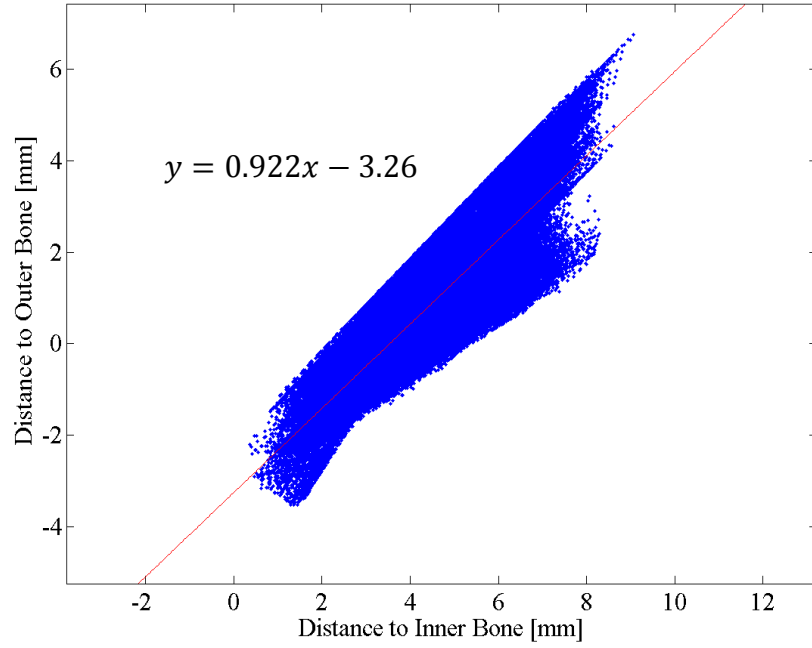
Figure 5.15: Minimum distance to the Outer bone vs. Maximum distance to the Inner Bone for Bone 1
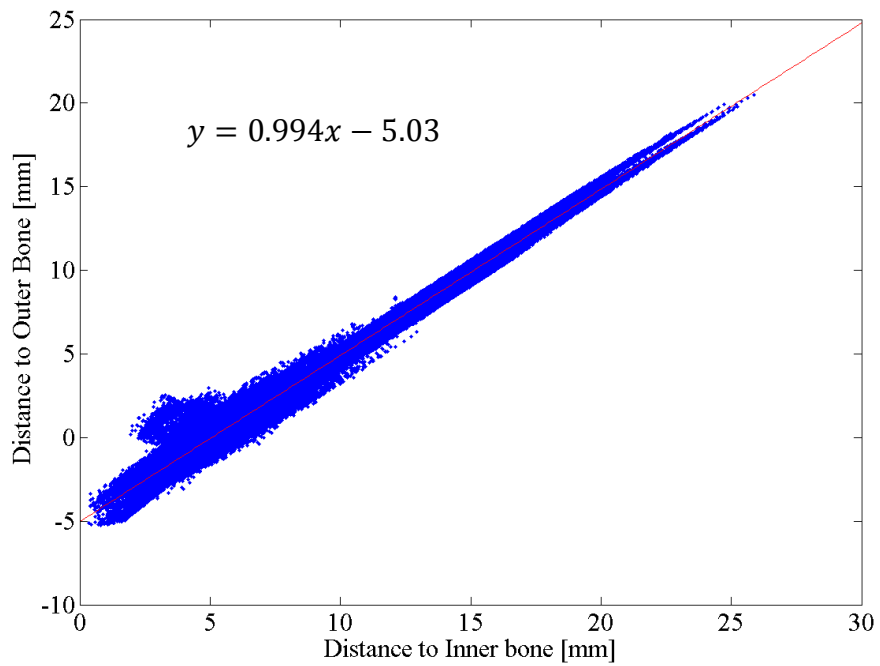
Figure 5.16: Minimum distance to the Outer bone vs. Maximum distance to the Inner Bone for Bone 2

$$y = 1.1x - 3.66$$
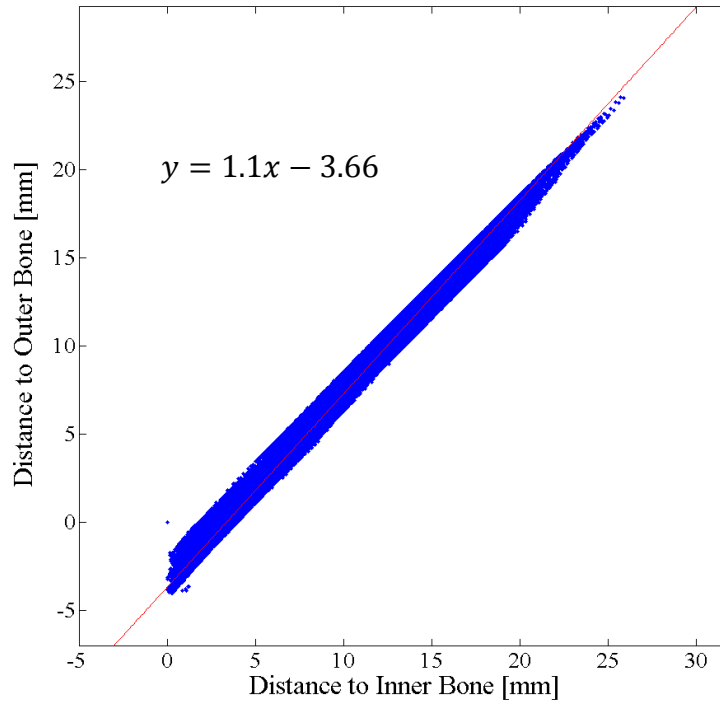
Figure 5.17: Minimum distance to the Outer bone vs. Maximum distance to the Inner
Bone for Bone 3

Evidentily, there exists a linear relationship between the distance to the outer bone

and the distance to the inner bone. The results presented in Table 5.2 show the statistical

analyses done on the linear line of best fit. The coefficient of determination represents

how much data is fittied on the linear line within the standard deviation. A value of 1

means that 100% of the data is fitted on the line of best fit within the standard deviation.

Analysis of variance (ANOVA) quantifies how well the fitted line 'fits' the data obtained.

Table 5.2: Results of the regression line fitting the maximum distance to the inner vs.
maximum distance to the outer bone for 3 bone samples

Bone Sample	Total sum of the squares (SST) [mm^2]	Error sum of squares (SSE) [mm^2]	Coefficient of determination (R^2)
1	665151	122500	0.816
2	4539934	62505	0.986
3	5575648	81504	0.985

From the ANOVA results, it can be concluded that minimizing the amount of interference of the implant stem will also maximize the amount of bone left over. In other words, minimizing the penetration distance to the inner bone will result in a thicker cortical humeral bone. Therefore, there is little need to consider simulateneously the distance to the outer bone and the distance to the inner bone. Thus minimizing the interference between the implatn stem and the inner bone boundary also maximizes the amount of cortical bone left over, or the distance to the outer bone.

Figure 5.18-Figure 5.20 show the pareto curves of all three bone samples. The blue dots in the graphs represents the implant positions tested during the algorithm. The global search technique was used for each specimen and the red dot indicates the converged implant position solution. Equal weights were assumed for the interference and malalignment objectives outlined in section 5.5. The first figure for each specimen showsall of the values tested whereas the second figure shows a zoomed in version where you can see the shape of the pareto curve more effectively.
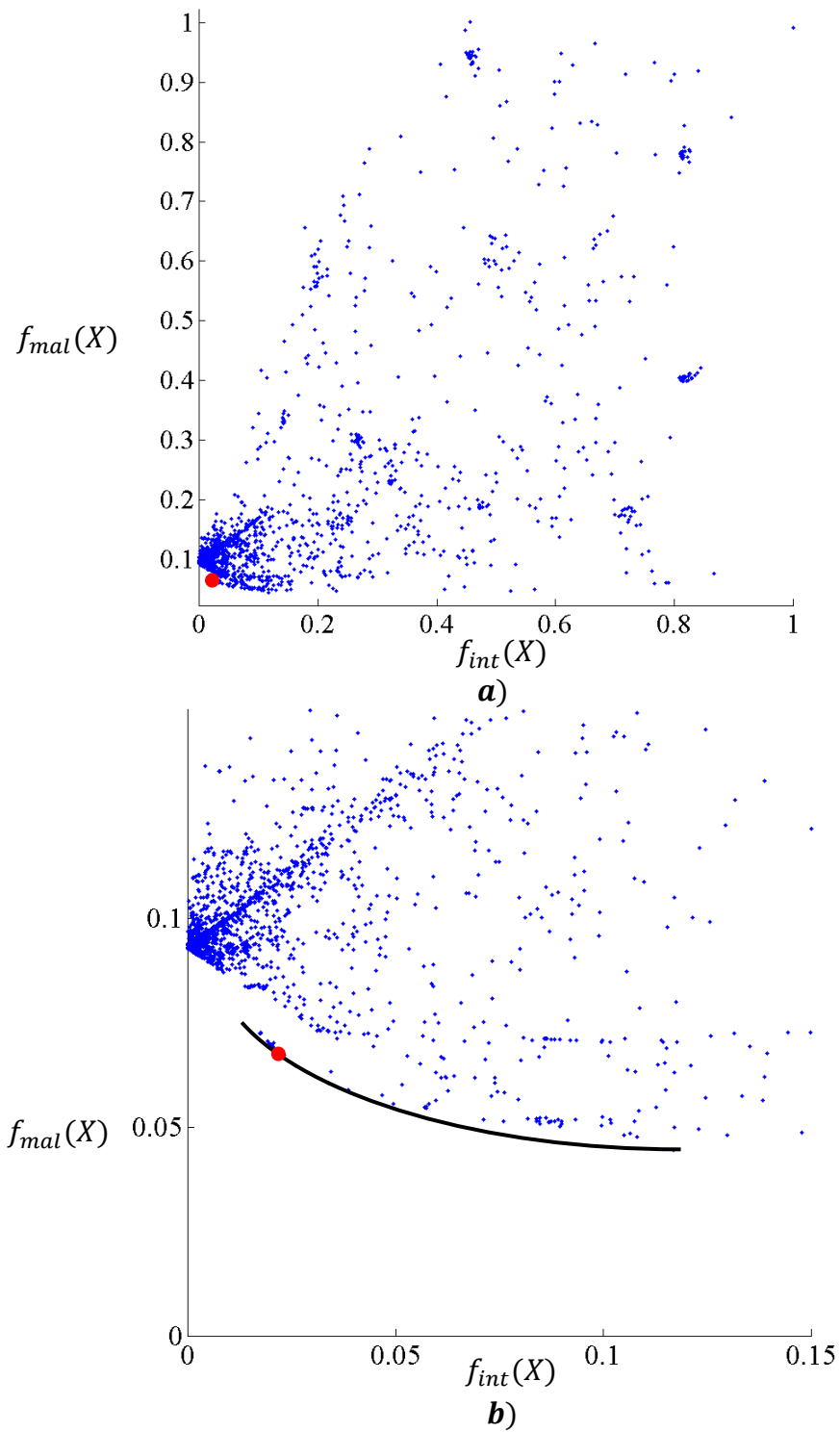
Figure 5.18: **a)** Pareto curve optimizing the position of the implant for bone sample 1. **b)** Zoomed in view. Each blue dot represents a unique implant position within the bounds provided. The red dot indicated the optimized solution with equal weights for the malalignment and interference objectives.
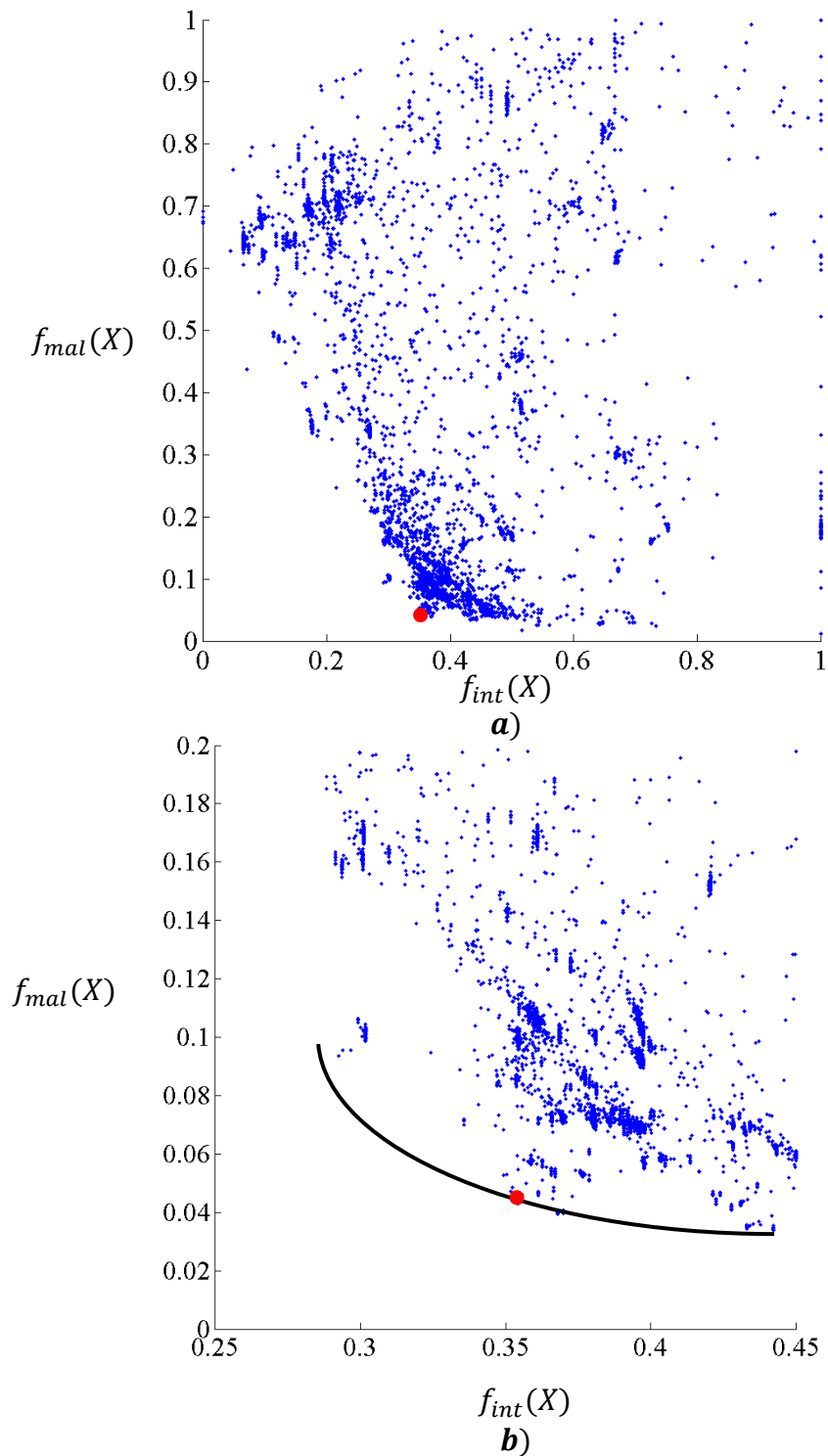
Figure 5.19: **a)** Pareto curve optimizing the position of the implant for bone sample 2. **b)** Zoomed in view. Each blue dot represents a unique implant position within the bounds provided. The red dot indicated the optimized solution with equal weights for the malalignment and interference objectives.
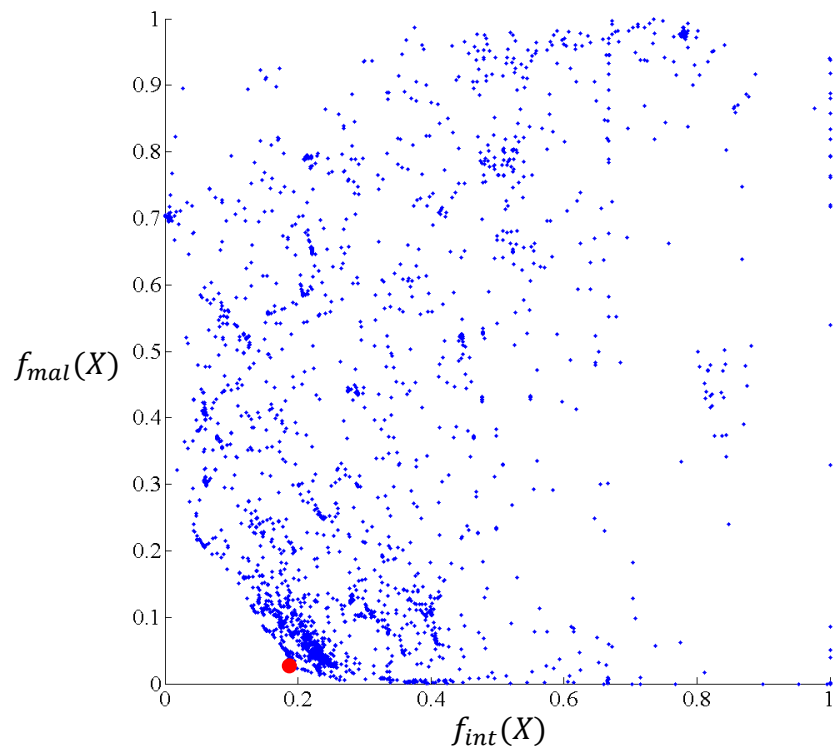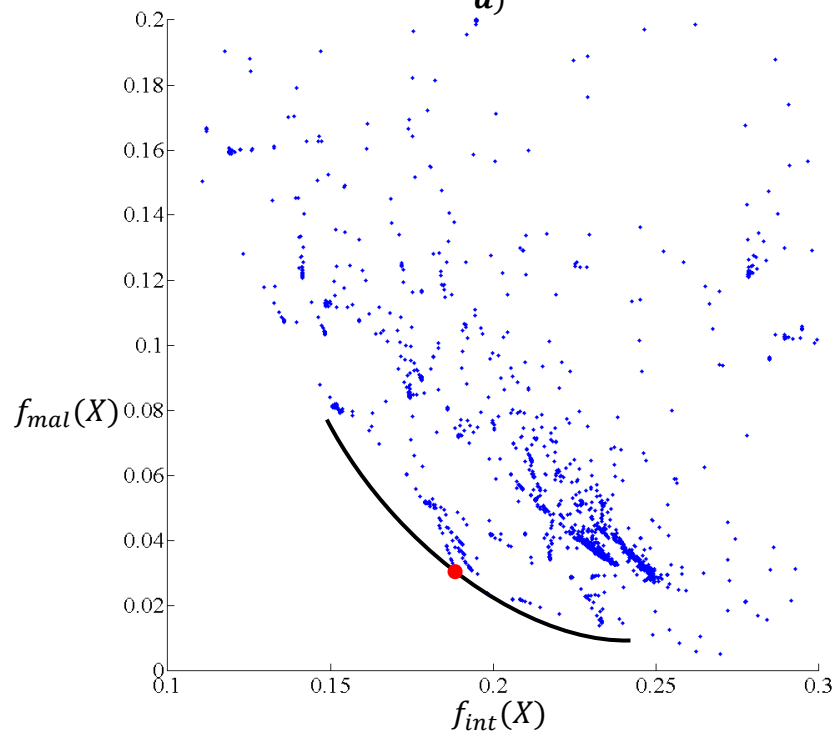
Figure 5.20: **a)** Pareto curve optimizing the position of the implant for bone sample 3. **b)** Zoomed in view. Each blue dot represents a unique implant position within the bounds provided. The red dot indicated the optimized solution with equal weights for the malalignment and interference objectives.

These results show that the algorithm effectively minimized the amount of interference between the implant stem and the medullary canal while simultaneously minimizing the amount of malalignment between the implant flexion-extension axis and the native flexion extension axis. If the surgeon were to pick different weights on the objective functions, different solutions would result. However, the solution would lie along the Pareto front in the figures presented above. If there were more of a weight on the malalignment objective rather than the interference objective, the solution would converge at a position that minimizes the malalignment objective at the cost of increasing the interference objective. In these figures, this change in weight would result in a converged solution point to the lower right of the indicated red points in the curve.

CHAPTER 6
CONCLUSIONS

6.1 OVERVIEW

One of the primary goals of the preoperative planning activities associated with TEA is the determination of the appropriate actions to be taken in order to minimize the malalignment between native and prosthetic FE axes of articulation. It is well known that implant malalignment causes eccentric loading through the joint leading eventually to implant loosening. If this occurs, subsequent revision surgeries are typically required and they pose further physical and emotional strain on TEA patients.

In order to provide orthopaedic surgeons with viable means to keep implant malalignment under control, the present study has developed computational tools whose overall goal is to indicate the location and minimal amount of cortical bone to be removed to ensure a superior positioning of the humeral stem. If successfully implemented in practice, these measures have the potential to eliminate or at least reduce the need for revision surgeries to ultimately translate into an improved quality of live for TEA patients.

A two-step approach was used during the development of the intended numerical techniques. During the first step, after the preliminary phase related to the extraction/determination of the discrete geometric representations for both implant stem and humeral bone contours, a one-dimensional Cartesian distance-based metric was introduced to quantify the amount of interference between the stem and cortical bone.

Then, by using either "brute-force" or global search optimization algorithms, constrained implant postures which allow minimization of the bone/implant interference were determined. It is anticipated that preoperative visualization of the interference zones will enable the surgeons to make educated decisions rather than guesses with respect to location of the cortical bone to be removed during canal reaming operations.

During the second step of development, the implant posture – initially treated as an input variable – became the second objective function to be minimized in addition to the amount of implant/bone interference. A more comprehensive volumetric metric was created to better quantify the amount of interference between the stem and humeral canal wall. According to the general theoretical framework related to the optimization of multiple objectives, regardless of the numerical method used to minimize the weighted objective function – *e.g.* global search, "brute force" or genetic algorithm – is was practically impossible to identify a unique "best" solution. Thus, the Pareto charts were generated in this context to demonstrate clearly the wide variety of optimal solutions possible. While in the context of the present work, equal importance has been assigned to both objective functions. It remains that future studies – performed perhaps in a clinical setting – are necessary to help the surgeon decide if a particular combination of weight factors would better suit the overall goal of the TEA procedure.

As an overall conclusion of the thesis, it can be stated that the broad anatomical variety in the geometry of the medullary canal, combined with the limited options available in terms of humeral implant design, generally prevent the achievement of a perfect alignment between native and prosthetic FE axis. While this situation can be partially corrected through bone removal, this operation has to be performed on the

highly conservative side in order to not substantially decrease the intrinsic strength of the bone. As such, the clear tradeoff which exists between the malalignment amount and the amount of interference between implant and bone can be solved by means of numerical methods similar to those developed in the context of this work.

6.2   LIMITATIONS

While the methodological correctness of the developed computational tools can, to a larger extent, be warranted, a number of built-in inaccuracies could potentially affect the precision of the numerical values outputted. In this regard, there are several sources of errors that can be cited, most of them being related to the accuracy used to generate the point-based representations of the bone. It should be reminded here that this process involves a succession of registration/orientation, acquisition/segmentation and polygon generation which could all be affected to a various extent by errors. While in the context of the present work, all of these errors were assumed nil, as they would become important while being transferred a quantitative manner to the surgeon or a robotic-assisted device.

In terms of registration/orientation of the humeral sample, the entire work was performed in the assumption that CT scanning planes are perpendicular to the longitudinal shaft of the humerus. While the convoluted shape of the medullary canal of the humerus makes this "perpendicularity" a slightly imprecise notion, this condition could be interpreted as the "minimal cross sectional area". In order words, the sample should be oriented during CT scanning in such a way to ensure that for each point along the Z-axis of the scanning/sample, the CT planes used are those characterized by a minimal cross sectional area. While the current work was entirely performed on

cadaveric specimens that were registered to a fixed coordinate system by means of trackers (flock of birds), this procedure would be difficult in the case of a patient. Obviously, the actual registration procedure is a process affected by its own intrinsic errors which could amount up to 1.9 ± 1 mm[72].

In terms of acquisition/segmentation errors, it should be mentioned that regardless of the complexity of the thresholding technique used, this process will be inherently affected by a number of errors, primarily caused by the loss of information during CT scanning. In other words, the digital image of the object generated as a result of CT scanning will inevitably represent nothing but an approximate representation of the humeral sample scanned. Arguably, the amount of dimensional errors – and thus the amount of lost information – can be decreased through a corresponding increase in the power of the scanner, but this does not represent a viable option while performing the procedure on patients. For this reason, the CT images used throughout the present work were acquired with the same parameters as those used in a clinical study, although dimensional deviations of up to 0.7 mm between digital and real artifacts can be expected in this case.

Finally, the polygonal approximation performed will introduce a small, but nonzero amount of "chordal" error with respect to the real geometry of the humeral sample. The smallest of the three types of errors mentioned, this type of error becomes important especially in the context of interference determination since the "binning" technique used to determine inner polygonal errors resulted in a decreased resolution for the corresponding polygons.

Moving forward, even if all these errors would be contained, the surgeons will be unable to follow these bone removal and implant positioning directions without the use of advanced visualization and navigational devices that are capable to accurately display in real time the amount of bone removed as well as the instantaneous posture of the implant during TEA. While some experimental progress has been made on the latter category, more efforts will be needed to bring these techniques to the OR.

Therefore, the variety of the errors listed in this section suggests that while the accuracy of the numerical values computed by the developed techniques can be questioned, they can be undoubtedly used in a qualitative sense since they can provide surgeons with a better idea of bone regions that should be machined in order to allow a superior implant positioning.

6.3 FUTURE DIRECTIONS

One of the first areas of improvement for the future should be precisely focused on the reduction of all the errors listed in the previous section. In the event that the intrinsic precision of bone reconstruction will increase to the level at which a higher degree of confidence exists in the numerical values generated, this type of computational techniques will also become interesting for the robotic-assisted surgical area since it will provide a valuable target to be achieved during the TEA. The same also holds true for surgeon-performed procedures since tracking devices of the implant and bone removal tools will eventually enable real time predictions of the results which are otherwise difficult to visualize.

It should be mentioned that the experimental validation of the results generated with these techniques is relatively difficult – especially when attempting to maintain high levels of precision. For this reason, it was not attempted during the limited tenure of this work. However, such validations of this work would add extra value to the theoretical premises built in this work and a broad variety of methods could be investigated. By starting off with simple CT visible "paint touchups" of the inner canal and ending with more sophisticated instrumented bench-top approaches to simultaneously track the position of the bone removal tool as well as that of the implant inserted in the canal. While the easiest way to assess the amount of material removed requires a CT scan to be performed after the canal reaming procedure, more precise alternate methods can also be envisioned. For example: post-reaming slicing of the specimen followed by hard measurements or the involvement of other noncontact measurement tools to assess post-reaming bone thickness (*e.g.* ultrasound).

Since the amount of bone removed is inherently associated with the amount of cutting force experienced during the procedure, more indirect measurement methods can also be imagined. However, the amount of cutting force represents a valuable piece of information in itself, since it can be used as a feedback signal during any type of surgical TEA procedure, regardless if performed by a human operator or a robotic-assisted device.

Finally, the extrapolation of these results to other types of analogous surgical procedures in which a longer prosthetic stem is required is also possible. The most likely candidates in this category are hip and knee replacements, although it should be stated that the relatively simple shape of the involved medullary canals might not justify the need for such in-depth investigations.

To conclude, while various advanced surgical procedures in which enhanced versions of developed tools might become useful, it would be reasonable to state here that the present lack of guidance with respect to bone reaming operation during TEA could be – at least to some extent – alleviated through the qualitative use of the tools developed in the context of this thesis.

APPENDIX

1	Separate Point cloud into CT slice data sets
2	Clean the data points in between CT slices
3	Determine the amount of CT slices
4	Determine minimum x-point in each CT slice
5	Triangulate the data
6	Determine minimum x-point neighbour
7	Separate neighbours into outer Bone matrix
8	Separate neighbours into outer Bone matrix
9	Divide inner bone into 40 bins

10	Check to see if 3 points are in each bin	No →	Decrease bin number by 1
11	Determine maximum and minimum		
12	Join maximum points followed by minimum points		
13	Separate inner bone polygon from point cloud		
14	Continue steps on all CT slices		

Yes

Figure A.1: Segmentation block diagram

```
        ┌─────────────────┐                        ┌─────────────────┐
        │  Identify critical│                      │    Determine     │
    1   │ implant points in│                   9  │  corresponding   │
        │       CAD        │                      │ implant geometry │
        └─────────────────┘                        └─────────────────┘
                 │                                          │
        ┌─────────────────┐                        ┌─────────────────┐
        │  Import point file│                      │ Determine implant│
    2   │   into MATLAB    │                  10  │ interference per │
        └─────────────────┘                      │  implant slice   │
                 │                                 └─────────────────┘
        ┌─────────────────┐                        ┌─────────────────┐
        │ Translate Implant│                      │   Sum up the     │
    3   │  FE Axis to Bone │                  11  │ interfering implant│
        │     FE Axis      │                      │     areas        │
        └─────────────────┘                        └─────────────────┘
                 │                                          │
        ┌─────────────────┐                        ┌─────────────────┐
        │  Rotate Implant FE│                      │ Sum up the entire│
    4   │ Axis to Bone FE  │                  12  │  implant cross   │
        │      Axis        │                      │    sections      │
        └─────────────────┘                        └─────────────────┘
                 │                                          │
        ┌─────────────────┐                        ┌─────────────────┐        ┐
        │ Define Implant   │                      │ Determine volume │        │
    5   │ translations and │                  13  │  of interference │        │
        │ rotations (6 DOF)│                      └─────────────────┘        │
        └─────────────────┘                                │                  │    ┌─────────────┐
                 │                                 ┌─────────────────┐        │    │  Outputs of │
        ┌─────────────────┐                        │    Determine     │        │    │ optimization│
        │   Spherical      │                      │   normalized     │        ├──  │ algorithms to│
        │   coordinate     │                  14  │   malalignment   │        │    │  determine  │
    6   │  translation to  │                      │     amount       │        │    │  optimized  │
        │   Cartesian      │                      └─────────────────┘        │    │  position   │
        │  coordinates     │                                │                  │    └─────────────┘
        └─────────────────┘                        ┌─────────────────┐        │
                 │                                 │ Determine double │        │
        ┌─────────────────┐                   15  │ objective function│       │
        │ Apply rotations  │                      │     value        │        │
    7   │ and translations │                      └─────────────────┘        ┘
        │ to implant points│
        └─────────────────┘
                 │
        ┌─────────────────┐
        │ Form parametric  │
    8   │ lines from critical│
        │ implant points   │
        └─────────────────┘
```
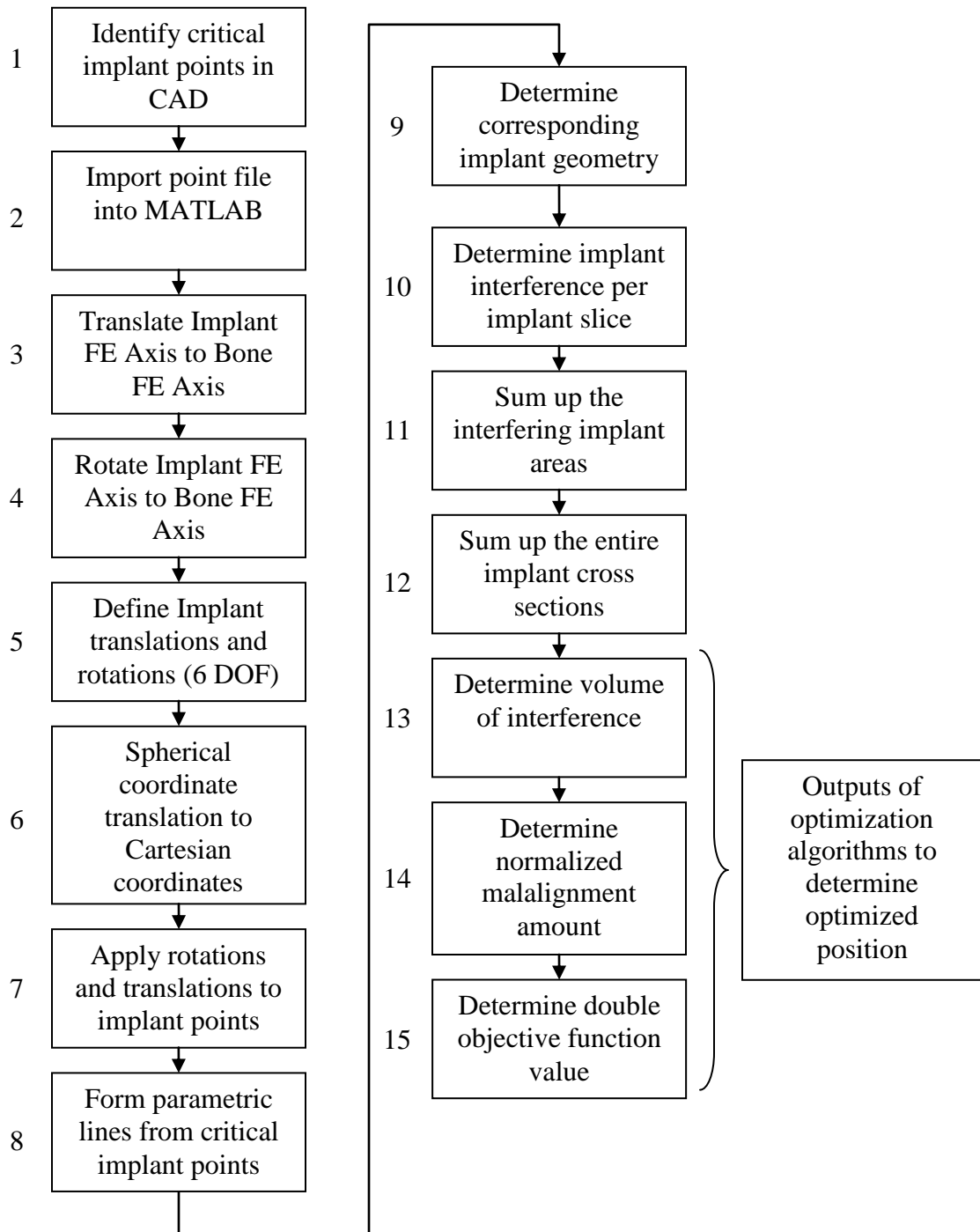
Figure A.2: Implant interference amount block diagram

95

REFERENCES

[1] Brownhill, J., Pollock, J., Ferreira, L., Johnson, J., & King, G. (2012). The effect of implant malalignment on joint loading in total elbow arthroplasty: an in vitro study. *Journal of Shoulder and Elbow Surgery, 21*(8), 1032--1038.

[2] Mora-Navarro, N., & Sánchez-Sotelo, J. (2012). Artroplastia de codo. *Revista Española de Cirugía Ortopédica y Traumatología*, *56*(5), 413-420.

[3] Lee, D. H. (2013). Reliability and Accuracy of Templating Humeral and Ulnar Components for Total Elbow Arthroplasty. *American Journal of Orthopedics*.

[4] Day, J., Lau, E., Ong, K., Williams, G., Ramsey, M., & Kurtz, S. (2010). Prevalence and projections of total shoulder and elbow arthroplasty in the United States to 2015. *Journal of Shoulder and Elbow Surgery, 19*(8), 1115--1120.

[5] Brownhill, J., Ferreira, L., Pichora, J., Johnson, J., & King, G. (2009). Defining the flexion-extension axis of the ulna: implications for intra-operative elbow alignment. *Journal of biomechanical engineering, 131*(2).

[6] Brownhill, J., King, G., & Johnson, J. (2007). Morphologic analysis of the distal humerus with special interest in elbow implant sizing and alignment. *Journal of Shoulder and Elbow Surgery , 16* (3), S126--S132.

[7] Stokdijk, M., Meskers, C. G. M., Veeger, H. E. J., De Boer, Y. A., & Rozing, P. M. (1999). Determination of the optimal elbow axis for evaluation of placement of prostheses. *Clinical Biomechanics*, *14*(3), 177-184.

[8] McDonald, C., Peters, T., Johnson, J., & King, G. (2011). Stem abutment affects alignment of the humeral component in computer-assisted elbow arthroplasty. *Journal of Shoulder and Elbow Surgery, 20*(6), 891--898.

[9] Brownhill, J. R., Mcdonald, C. P., Ferreira, L. M., Pollock, J. W., Johnson, J. A., & King, G. J. (2012). Kinematics and laxity of a linked total elbow arthroplasty following computer navigated implant positioning. *Computer Aided Surgery*, *17*(5), 249-258.

[10] Celli, A., & Morrey, B. (2009). Total elbow arthroplasty in patients forty years of age or less. *The Journal of Bone \& Joint Surgery, 91*(6), 1414--1418.

[11] Chalidis, B., Dimitriou, C., Papadopoulos, P., Petsatodis, G., & Giannoudis, P. (2009). Total elbow arthroplasty for the treatment of insufficient distal humeral fractures. A retrospective clinical study and review of the literature. *Injury, 40*(6), 582--590.

[12] Fevang, B.-T., Lie, S., Havelin, L., Skredderstuen, A., & Furnes, O. (2009). Results after 562 total elbow replacements: a report from the Norwegian Arthroplasty Register. *Journal of Shoulder and Elbow Surgery, 18*(3), 449--456.

[13] Kim, J., Mudgal, C., Konopka, J., & Jupiter, J. (2011). Complications of total elbow arthroplasty. *Journal of the American Academy of Orthopaedic Surgeons, 19*(6), 328--339.

[14] Krenek, L., Farng, E., Zingmond, D., & SooHoo, N. (2011). Complication and revision rates following total elbow arthroplasty. *The Journal of hand surgery, 36*(1), 68--73.

[15] Sanchez-Sotelo, J., & Morrey, B. (2011). Total elbow arthroplasty. *Journal of the American Academy of Orthopaedic Surgeons, 19*(2), 121--125.

[16] Abdel, M., & Morrey, B. (2010). Implications of revision total elbow arthroplasty on blood transfusion. *Journal of shoulder and elbow surgery, 19*(2), 190--195.

[17] Throckmorton, T., Zarkadas, P., Sanchez-Sotelo, J., & Morrey, B. (2010). Failure patterns after linked semiconstrained total elbow arthroplasty for posttraumatic arthritis. *The Journal of Bone \& Joint Surgery, 92*(6), 1432--1441.

[18] Dean, G., Holliger IV, E., & Urbaniak, J. (1997). Elbow Allograft for Reconstruction of the Elbow With Massive Bone Loss; Long Term Results. *Clinical orthopaedics and related research, 341*, 12--22.

[19] Morrey, B. F., & Sanchez-Sotelo, J. (Eds.). (2009). *The elbow and its disorders*. Elsevier Health Sciences.

[20] Kai-Nan An, M. E. (2009). Biomechanics of the Elbow. In J. S.-S. Bernard Morrey, *The Elbow and its Disorders* (pp. 39-63). Philidalphia: Elsevier.

[21] Duck, T., Dunning, C., Armstrong, A., Johnson, J., & King, G. (2003). Application of screw displacement axes to quantify elbow instability. *Clinical Biomechanics, 18*(4), 303--310.

[22] Duck, T., Dunning, C., King, G., & Johnson, J. (2003). Variability and repeatability of the flexion axis at the ulnohumeral joint. *Journal of orthopaedic research, 21*(3), 399--404.

[23] Fornalski, S., Gupta, R., & Lee, T. Q. (2003). Anatomy and biomechanics of the elbow joint. *Techniques in Hand & Upper Extremity Surgery*, *7*(4), 168-178.

[24] Brownhill, J., Furukawa, K., Faber, K., Johnson, J., & King, G. (2006). Surgeon accuracy in the selection of the flexion-extension axis of the elbow: an in vitro study. *Journal of shoulder and elbow surgery, 15*(4), 451--456.

[25] Morrey, B. F., & Chao, E. Y. (1976). Passive motion of the elbow joint. *J Bone Joint Surg Am*, *58*(4), 501-508.

[26] McDonald, C. (2008). *Image-Guided surface-based registration of the elbow.* London, Ontario, Canada: Library and Archives Canada.

[27] Schuind, F., O'Driscoll, S., Korinek, S., An, K., & Morrey, B. (1995). Loose-hinge total elbow arthroplasty: an experimental study of the effects of implant alignment on three-dimensional elbow kinematics. *The Journal of arthroplasty, 10*(5), 670--678.

[28] Podgorski A., K. B. (2012). Biomechanical assessment of varus-valgus range of motion of normal elbow joint using prototype measuring device. *Ortop Traumatol Rehabil*, 137-44.

[29] Tornier. (2013). *Latitude EV Total Elbow Prosthesis*. Retrieved May 2013, from http://www.tornier-us.com/upper/elbow/elbrec001/index.php?pop=1

[30] Bharath, A. A. (2009). *Introduction to Medical Imaging*. Morgan & Claypool Publishers.

[31] Prokop, M., & Galanski, M. (Eds.). (2003). *Spiral and multislice: computed tomography of the body*. George Thieme Verlag.

[32] Robert H. Choplin, J. M. (1992). Picture Archiving nad Communcation Systems: An Overview. *Radiographs*, 127-129.

[33] National Electrical Manufacturers Association. (n.d.). *DICOM Homepage*. Retrieved 07 2013, 2013, from DICOM: http://medical.nema.org/standard.html

[34] Gregory, J., Ennis, O., & Hay, S. (2008). (ii) Total elbow arthroplasty. *Current Orthopaedics, 22*(2), 80--89.

[35] Ikävalko, M., Tiihonen, R., Skyttä, E., & Belt, E. (2010). Long-term survival of the Souter-Strathclyde total elbow replacement in patients with rheumatoid arthritis. *Journal of Bone \& Joint Surgery, British Volume, 92*(5), 656--660.

[36] McDonald, C., Johnson, J., Peters, T., & King, G. (2010). Image-based navigation improves the positioning of the humeral component in total elbow arthroplasty. *Journal of Shoulder and Elbow Surgery, 19*(4), 533-543.

[37] O Driscoll, S., Jupiter, J., King, G., Hotchkiss, R., & Morrey, B. (2001). The unstable elbow. *INSTRUCTIONAL COURSE LECTURES-AMERICAN ACADEMY OF ORTHOPAEDIC SURGEONS, 50*, 89--104.

[38] Tutunea-Fatan, O. R., Bernick, J. H., Lalone, E., King, G. J., & Johnson, J. A. (2010, March). Application of collision detection to assess implant insertion in elbow replacement surgery. In *SPIE Medical Imaging* (pp. 76251K-76251K). International Society for Optics and Photonics.

[39] Frölke, J. P. (2006). Intramedullary Reaming of Long Bones. In *Practice of Intramedullary Locked Nails* (pp. 43-56). Springer Berlin Heidelberg.

[40] Dee, R. (1972). Total replacement arthroplasty of the elbow for rheumatoid arthritis. *J Bone Joint Surg Br*, *54*(1), 88-95.

[41] Chafik, D., & Gupta, R. (2002). Primary total elbow arthroplasty. *Operative Techniques in Orthopaedics, 12*(1), 15--20.

[42] Chapman, M. (1998). The effect of reamed and nonreamed intramedullary nailing on fracture healing. *Clinical orthopaedics and related research, 355*, S230--S238.

[43] Tsai, M.-D., Hsieh, M.-S., & Tsai, C.-H. (2007). Bone drilling haptic interaction for orthopedic surgical simulator. *Computers in Biology and Medicine, 37*(12), 1709--1718.

[44] Aldridge, J. M., Lightdale, N. R., Mallon, W. J., & Coonrad, R. W. (2006). Total elbow arthroplasty with the Coonrad/Coonrad-Morrey prosthesis A 10-TO 31-YEAR SURVIVAL ANALYSIS. *Journal of Bone & Joint Surgery, British Volume*, *88*(4), 509-514.

[45] Kraay, M. J., Figgie, M. P., Inglis, A. E., Wolfe, S. W., & Ranawat, C. S. (1994). Primary semiconstrained total elbow arthroplasty. Survival analysis of 113 consecutive cases. *Journal of Bone & Joint Surgery, British Volume*, *76*(4), 636-640.

[46] Little, C. P., Graham, A. J., & Carr, A. J. (2005). Total elbow arthroplasty A SYSTEMATIC REVIEW OF THE LITERATURE IN THE ENGLISH LANGUAGE UNTIL THE END OF 2003. *Journal of Bone & Joint Surgery, British Volume*,*87*(4), 437-444.

[47] Schneeberger, A. G., Meyer, D. C., & Yian, E. H. (2007). Coonrad-Morrey total elbow replacement for primary and revision surgery: a 2-to 7.5-year follow-up study. *Journal of Shoulder and Elbow Surgery*, *16*(3), S47-S54.

[48] F.C. Ewald, R. S. (1980). Capitellocondylar Total Elbow Arthroplasty. *Jounral of Bone and Joint Surgery*, 1259-1263.

[49] Thomas Trancik, A. H. (1991). Capitellocondylar Total Elbow Arthroplasty. *Clinical Orthopaedics and Related Research*, 175-180.

[50] Tomasz K. W. Kozak, R. A. (2009). Total Elbow Arthroplast for Primary Osteoarthritis. In J. S.-S. Bernard F. Morrey, *The Elbow and its Disorders* (pp. 843-861). Philadelphia: Elsevier.

[51] Morrey, B. F., & Adams, R. A. (1992). Semiconstrained arthroplasty for the treatment of rheumatoid arthritis of the elbow. *The Journal of bone and joint surgery. American volume*, *74*(4), 479-490.

[52] Kasten, M. D., & Skinner, H. B. (1993). Total Elbow Arthroplasty An 18-Year Experience. *Clinical orthopaedics and related research*, *290*, 177-188.

[53] Norbert Gschwent, B. R. (1996). Late complications in elbow arthroplasty. *Journal of Shoulder and Elbow Surgery*, 86-96.

[54] Lorensen, W., & Cline, H. (1987). Marching cubes: A high resolution 3D surface construction algorithm. *ACM Siggraph Computer Graphics*, *21*, pp. 163--169.

[55] Kitware Inc. (2006). VTK User's Guide Version 5. Clifton Park, New York.

[56] Coello, C. A. C., & Lamont, G. B. (Eds.). (2004). *Applications of multi-objective evolutionary algorithms* (Vol. 1). World Scientific.

[57] Zeid. I.(2004). Mastering CAD/CAM, *McGraw-Hill*. New York, NY, USA.

[58] Glover, F. (1998). A template for scatter search and path relinking. *Artificial evolution*, (pp. 1-51).

[59] MathWorks, (2012). *Global Optimization Toolbox: User's Guide (R2012b)*. Retrieved July 14, 2012 from http://www.mathworks.com/products/global-optimization/

[60] Schaffler, S. (2012). Global Optimization. Springer, NY.

[61] Ugray, Z., Lasdon, L., Plummer, J., Glover, F., Kelly, J., & Mart\\i, R. (2007). Scatter search and local NLP solvers: A multistart framework for global optimization. *INFORMS Journal on Computing, 19*(3), 328--340.

[62] Hormann, K., & Agathos, A. (2001). The point in polygon problem for arbitrary polygons. *Computational Geometry*, *20*(3), 131-144.

[63] Tingart, M. J., Apreleva, M., von Stechow, D., Zurakowski, D., & Warner, J. J. P. (2003). The cortical thickness of the proximal humeral diaphysis predicts bone mineral density of the proximal humerus. *Journal of Bone & Joint Surgery, British Volume*, *85*(4), 611-617.

[64] Kumar, M., Husian, M., Upreti, N., & Gupta, D. (2010). Genetic algorithm: Review and application. *International Journal of Information Technology and Knowledge Management*, *2*(2), 451-454.

[65] Burke, E. K., & Kendall, G. (Eds.). (2005). *Search methodologies: introductory tutorials in optimization and decision support techniques*. Springer.

[66] Ge, A. W., & Jackson, R. L. (2013). *U.S. Patent No. 8,428,335*. Washington, DC: U.S. Patent and Trademark Office.

[67] Pankratov, K. K. (1995). *Polybool Boolean Operators on Polygons*. pp. 1-5

[68] Glassner, A. S. (1990). Graphics gems. Academic Press, Inc..

[69] Arvo, J. (Ed.). (1991). Graphics Gems Two (Vol. 2). Morgan Kaufmann.

[70] De Berg, M., Van Kreveld, M., Overmars, M., & Schwarzkopf, O. C. (2000). Computational geometry (pp. 1-17). Springer Berlin Heidelberg.

[71] Holland, J. H. (1975). *Adaptation in natural and artificial systems: An introductory analysis with applications to biology, control, and artificial intelligence*. U Michigan Press.

[72] Mcdonald, C. P., Brownhill, J. R., King, G. J., Johnson, J. A., & Peters, T. M. (2007). A comparison of registration techniques for computer-and image-assisted elbow surgery. Computer Aided Surgery, 12(4), 208-214.

CURRICULUM VITAE

Name: Alexander James Heroux

Post-secondary   University of Western Ontario
Education and   London, Ontario, Canada
Degrees: 2006-2011 B.E.Sc.

                             The University of Western Ontario
                             London, Ontario, Canada
                             2006-2011 B.Sc.

Related Work   Teaching Assistant
Experience   The University of Western Ontario
                             2011-2013

Publications:

Heroux, A.J., Tutunea-Fatan, O.R., Salisbury, S.P., Barari, A. 2013,"Minimization of Bone Removal Through Optimal Humeral Implant Alignment in Total Elbow Arthroplasty," accepted for publication in *Computer-Aided Design and Applications*.

Heroux, A.J., Tutunea-Fatan, O.R., Salisbury, S.P., Barari, A. 2013,"Minimization of Bone Removal Through Optimal Humeral Implant Alignment in Total Elbow Arthroplasty," USB Proceedings of the CAD'13 Conference, Jun. 2013, Bergamo, Italy, paper 72, 19 pages.

Heroux, A.J., Salisbury, S.P., and Tutunea-Fatan, O.R., 2012 "Minimization of the Interference Between Implant and Distal Humerus for Total Elbow Arthroplasty," poster presented at *London Health Research Day 2012*,
Mar. 2012, London, Canada.